

DeepLandforms: A Deep Learning Computer Vision toolset applied to a prime use case for mapping planetary skylights

Giacomo Nodjoumi¹, Riccardo Pozzobon², Francesco Sauro³, and Angelo Pio Rossi¹

¹Jacobs University Bremen

²Università degli Studi di Padova

³University of Bologna

November 25, 2022

Abstract

Thematic map creation is a process that implies several steps to be accomplished regardless of the type of the map to be produced, starting from data collection, through data exploitation and ending with maps publication as print, image, and GIS format. An example are geological, lithological, and geomorphological maps, in which most of the highest time-consuming tasks are those related to the discretization of single objects by identifying a set of unique characteristics that describe uniquely those objects. Commonly these tasks introduce interpretative biases due to the different experience of the mappers who's performing it. In this setting, Deep Learning Computer Vision techniques could play a key-role but lack the availability of a complete set of tools specific for planetary mapping. The aim of this work is to develop a comprehensive set of ready-to-use tools for landforms mapping, in which users have full access to the workflow and over all the processes involved, granting complete control and customization capabilities. In this work are presented both the developed tools and the approach that has been used and that is based on consolidated Deep Learning methodologies and open-source libraries commonly applied in other fields of Computer Vision. The toolset and the approach presented have been tested in the science case of mapping sinkhole-like landforms on Mars and results are presented.

1 **DeepLandforms: A Deep Learning Computer Vision toolset applied to a prime use case for mapping planetary skylights**

2

3 **Giacomo Nodjoumi^{1*}, Riccardo Pozzobon^{2,3}, Francesco Sauro⁴, Angelo Pio Rossi¹**

4 ¹Jacobs University Bremen gGmbH, Bremen, Germany

5 ²INAF-Astronomical Observatory of Padova, Padova, Italy

6 ³Department of Geosciences, University of Padova, Padova, Italy

7 ⁴Department of Biological, Geological and Environmental Sciences, University of Bologna, Bologna, Italy

8 Corresponding author: Giacomo Nodjoumi (g.nodjoumi@jacobs-university.de)

9 **Key Points:**

- 10
- Instance Segmentation methodology is used to map landforms obtaining vectorial data in geopackage file format.
- 11
- A newly developed composite toolset to perform the image pre-processing, data labeling, model training and inference tasks, is presented.
- 12
- The results of a prime case of mapping pit and skylights on Mars surface are showed.
- 13
- 14

15 Abstract

16 Thematic map creation is a process that implies several steps to be accomplished regardless of the type of the map to
17 be produced, starting from data collection, through data exploitation and ending with maps publication as print, image,
18 and GIS format. An example are geological, lithological, and geomorphological maps, in which most of the highest
19 time-consuming tasks are those related to the discretization of single objects by identifying a set of unique
20 characteristics that describe uniquely those objects. Commonly these tasks introduce interpretative biases due to the
21 different experience of the mappers who's performing it. In this setting, Deep Learning Computer Vision techniques
22 could play a key-role but lack the availability of a complete set of tools specific for planetary mapping. The aim of
23 this work is to develop a comprehensive set of ready-to-use tools for landforms mapping, in which users have full
24 access to the workflow and over all the processes involved, granting complete control and customization capabilities.
25 In this work are presented both the developed tools and the approach that has been used and that is based on
26 consolidated Deep Learning methodologies and open-source libraries commonly applied in other fields of Computer
27 Vision. The toolset and the approach presented have been tested in the science case of mapping sinkhole-like
28 landforms on Mars and results are presented.

29 Plain Language Summary

30 The creation of maps is a complex set of several tasks that, regardless of the type of the map, are often very time-
31 consuming. For instance, all the occurrences of a specific object, natural or man-made in a defined area, needs to be
32 identified, drawn and classified manually; a work that can be easily accomplished for large object in small areas but
33 may be unmanageable in cases such the mapping of small landforms on the entire surface of a planet or moon.
34 Nowadays, especially on Earth, several of the above tasks takes advantages of highly specialized computer codes
35 based on Deep Learning systems. Such codes are almost never ready-to-use, and require higher knowledge in
36 computer programming languages. In this work we present the first release of a novel open-source computer software,
37 almost ready-to-use, that provides all the instruments for creating or directly using custom Deep Learning models for
38 automatic landforms mapping. We present also the results obtained by trying this software using data of Mars's surface
39 with the aim of mapping sinkhole-like landforms.

40 1. Introduction

41 The exploration of terrestrial planets in the Solar System was and still is performed mainly on data that cover almost
42 all the electromagnetic spectrum, acquired over the last century by several types of orbiters, rovers, and landers.
43 Planetary data volumes are constantly increasing both in quality and quantity, with the contribution of both public and
44 private entities.

45 Imagery has always been the primary resource for researchers in planetary sciences, especially for geologists and
46 geomorphologists. In the last two decades the progress in the development of very high-resolution image sensors gave
47 access to the community to images with a spatial resolution in the order of centimeters. Data collected by High
48 Resolution Imaging Science Experiment (HiRISE) instrument, on board of the Mars Reconnaissance Orbiter (MRO)
49 (McEwen et al., 2007) or by the Narrow Angle Camera (NAC) experiment, on board of Lunar Reconnaissance Orbiter
50 (LRO) (Robinson et al., 2010), have been used in several works related on their planetary body.

51 These include not only publications related to specific surface's features such as the impact of megabreccia (Grant et
52 al., 2008), crater counting and morphometry (Benedix et al., 2020; Chen et al., 2017; Robbins & Hynes, 2014; Servis
53 et al., 2020; Watters et al., 2015), boulder counting (Le Mouélic et al., 2020; Sargeant et al., 2020; Watkins et al.,
54 2017) characterization of polar layered deposits (Milkovich et al., 2009), identification of the source of ice blocks in
55 the north polar cap (Su et al., 2021) but also comparative analyses and numerical modeling (Guimpier et al., 2021),
56 analyses of Mars's surface processes (Guallini et al., 2018; Luzzi et al., 2020) including skylight, pits (Barlow et al.,
57 2017; Cushing et al., 2015; Michikami et al., 2014; Xiao et al., 2014), pit chains (Wyrick, 2004) , and more advanced
58 application such as Structure-from-Motion (SfM), (Le Mouélic et al., 2020; Micheletti et al., 2015; Muller et al., 2021;
59 Y. Wang et al., 2021), Shapes-from-Shading (SfS) (Alexandrov & Beyer, 2018; Lohse et al., 2006), Machine Learning
60 for object detection and classification (Barrett et al., 2022; Dundar et al., 2019; Hipperson et al., 2020, 2020; Hu et
61 al., 2021; Lee, 2019; Nodjoumi et al., 2021; Palafox et al., 2017; Rashno et al., 2017; Silburt et al., 2019; Wilhelm et
62 al., 2020).

63 This leap in image quality and quantity has introduced new challenges for researcher since the higher resolutions
64 brought the great advantage of being able to analyze the surface of those planets with unprecedented details, retrieving
65 useful information of various field such the characterization of Martian and lunar pits (Cushing et al., 2015; Haruyama
66 et al., 2009; Kaku et al., 2017; Sharma & Srivastava, 2021; Wyrick, 2004; Xiao et al., 2014) or the Recurring Slope
67 Lineae (RSL) (McEwen et al., 2021), but with several downsides, for instance, larger image size ad numbers of
68 acquisitions available may create problems for large scale processing due to the computational power requirements.

69 Map production is a complex set of tasks performed by teams and groups of researchers specialized in single to
70 multiple fields that combine their knowledge in order to describe and characterize the surface of a planet
71 ('Geomorphological Mapping', 2013; Napieralski et al., 2013; Nass et al., 2021). Depending on the type of the map
72 in production, these tasks may vary a lot but at least four major focal tasks are shared across all map types: a) data
73 collection, b) data exploitation , c) map creation, d) map dissemination (Naß et al., 2017, 2021). Among those major
74 tasks, the most time-consuming sub-tasks are the definition of the standards for the map production and dissemination
75 (Hare et al., 2018) and the proper digital creation of the map elements by manual drawing all the features of the area
76 of interest using GIS software. For instance, in geomorphological mapping, the main target is the identification of
77 landforms. With the term landform, is intended a topographic expression of the surface of a planetary body that can
78 be described by at least seven parameters, shape, size, height, texture, pattern, tone/hue, location/association (Tempfli
79 et al., 2009) that combined generate a unique object while Multiple landforms in an area describe a terrain (Bridge &
80 Demicco, 2008; DiPietro, 2013). See Table S1 in supporting information.

81 Genetic mechanisms are a complex combination of interconnected processes and forces, some of which are more wide
82 and planetary-scale dependent. For instance gravity usually drives the size of different morphologies such as lava
83 tubes and rilles on the Moon, Mars and Earth (Bardabelias et al., 2020; Chappaz et al., 2017; Cruikshank & Wood,
84 1972; Greeley, 1971; Haruyama et al., 2009; Horvath et al., 2020; Kaku et al., 2017; Lèveillé & Datta, 2010; F. Sauro
85 et al., 2020; Whitten & Martin, 2019). Other mechanisms are more related to the presence of specific environmental
86 and atmospheric characteristics and may drive different subtypes of a common landform type.

87 Among the many examples, landforms such as landslides (Hung et al., 2014) and sinkholes (Parise, 2019) found on
88 Mars (Bardabelias et al., 2020; Cushing et al., 2007; De Blasio, 2011; Guimpier et al., 2021; Hooper & Smart, 2013;
89 Sharma & Srivastava, 2021), may have some formation and driving mechanisms in common to their respective
90 landforms found on Earth (Acharya et al., 2006; Díaz Michelena et al., 2020; Gutiérrez et al., 2008; Hung et al.,
91 2014; Jiang, 2020; Parise, 2019; U. Sauro, 2016; Van Den Eeckhaut et al., 2007; Youssef et al., 2012). Those
92 mechanisms and settings may be related to similar surface and subsurface characteristics and properties such as the
93 geological settings, type of substratum, the average slope, and the solar exposure of the area.

94 Conversely, the presence of liquid-water seasonal precipitation and groundwater circulation, on landslides and
95 sinkholes found on Earth is not only a driving mechanism but may also act as a trigger for the process (Allemand et
96 al., 2011; Alonso et al., 2010; Cahalan & Milewski, 2018; Díaz Michelena et al., 2020; Duhart et al., 2019; Gutiérrez
97 et al., 2008; Jiang, 2020; Lacerda et al., 2004; Lin et al., 2004; Van Den Eeckhaut et al., 2007; Youssef et al., 2012),
98 while it is still under debate on those found on Mars (De Blasio, 2011; Guimpier et al., 2021; Hooper & Smart, 2013;
99 Salese et al., 2019; Smith et al., 2006).

100 Several types of terrains and thus landforms exist, natural and artificial, some are peculiar to specific areas or even
101 planets or moons, others can be found in almost all planetary bodies of the Solar System (Hargitai & Kereszturi,
102 2015a).

103 In general terms, the occurrence of specific landforms are deeply connected to the geology of the area, the past and
104 present atmospheric processes and, at least on Earth, by anthropological activities (this applies to a certain extent also
105 to robotic or human landing sites) (Brierley et al., 2021; James et al., 2013; Slaymaker et al., 2021). Studying those
106 features is essential to better know the relations between those three main major processes and characteristics and the
107 evolution of the area.

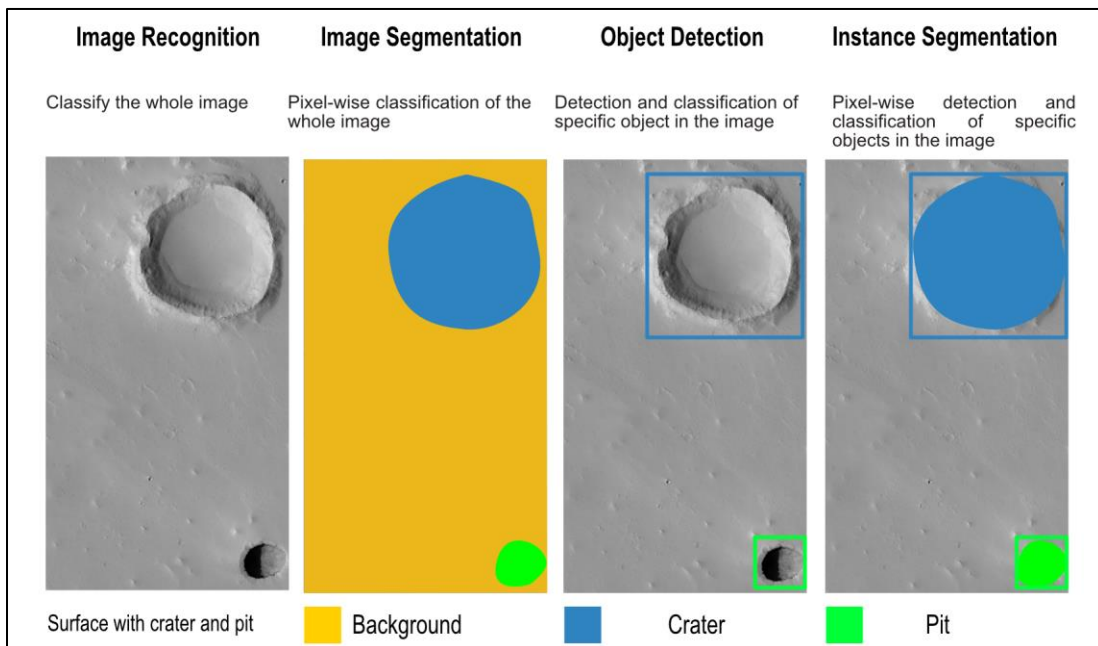
108 Identification, classification and description of landforms is done by mappers using multiple data types and sources
109 such as images in various spectra, previous maps, digital elevation models and so on (Luzzi et al., 2020; Parente et
110 al., 2019; Sivakumar et al., 2017). The time necessary to accomplish this specific sub-task is strictly dependent on the
111 scale of the area of interest and scale of the features in it since wider areas and smaller features may lead to extremely
112 high workloads. The final map product is a fundamental element to consider while estimating the complexity of the
113 map production work. This is due to the wide diversity of map products available, and thus to the parameters to be
114 defined and the data to be collected and processed

115 Indeed, geological maps takes into account spatial-temporal relations between surface and subsurface's features, their
116 compositions and the past and present geological processes involved (Martinot et al., 2018; Naß & van Gasselt, 2021;
117 Pondrelli et al., 2020; Sun & Stack, 2020; Tsibulskaya et al., 2020), while geomorphological maps takes the same
118 parameters at a higher level, more related to the visual properties derived by the acquired images like colors, texture,
119 patterns and so on (Kumar et al., 2019; Tirsch et al., 2021; Tsibulskaya et al., 2020; B. Wu et al., 2020).

120 In addition, regardless of the type of map, the data collection steps can be very time-consuming tasks, beyond being
121 also complex, since most of the available data needs to be pre-processed prior to the proper analysis. For example,
122 there are more than 1.8 million products of HiRISE acquisitions that are roughly more than 49 Terabyte for a single
123 imager that is still acquiring data at the time of writing.

124 In this framework, Deep Learning computer vision methodologies, are robust and widely accepted and applied both
 125 on Earth for crops monitoring and management (Grace et al., 2021), land use (Rousset et al., 2021; Talukdar et al.,
 126 2020), risk management and assessment (Ghorbanzadeh et al., 2019; Liu et al., 2004; Merghadi et al., 2020; Paul &
 127 Ganju, 2021; Tien Bui et al., 2016; Yousefi et al., 2020); and on other Solar System planetary body (Barrett et al.,
 128 2022; Dundar et al., 2019; Hipperson et al., 2020, 2020; Lee, 2019; Palafox et al., 2017; Rashno et al., 2017; Stepinski
 129 et al., 2007; S. Wang et al., 2020; Wilhelm et al., 2020); thus may be play a crucial role in exploiting such amount of
 130 data.

131 The objectives of these methodologies are mainly of four types listed below and shown in Figure 1.



132
 133 **Figure 1.** Comparison between image recognition, image segmentation, object detection and instance segmentation
 134 for the specific case of geomorphology mapping.

135 The first methodology displayed in Figure 1 is the *Image Recognition (ImR)* which classifies the whole image contents,
 136 the second, called *Image Segmentation (ImS)*, classifies each pixel of the image and create segments of adjacent pixels
 137 with contiguous classification. The third technique, the *Object Detection (OD)*, locate the objects using bounding
 138 boxes and classifies them separately, while the fourth, the *Instance Segmentation (InS)* is a combination of the second
 139 and the third method, obtaining the segmentation of only the objects identified by the detection.

140 Those architectures may require a tremendous amount of well labeled training data in order to generalize properly the
 141 model and avoid overfitting and underfitting problems (Zhang et al., 2021). More detailed descriptions are available
 142 in the supporting information Text S1.

143 Such data, are not always ready-to-use for labeling, mostly due to compatibility issues between labeling software,
 144 deep learning software and data itself. More specifically, these issues are related mainly to data size and format, and
 145 therefore pre-processing tasks have a key role and are mandatory for any approach especially if georeferencing

146 information is required. A more detailed overview is provided in the supporting information Text S3 along with
147 detailed pre-processing steps.

148 Nowadays, Deep Learning methodologies are widely and commonly used as a solution to solve several daily problems,
149 for instance facial recognition features of social networks, Google images search, security surveillance and much
150 more, but also specific problems relative to Earth Observation such as land coverage, crops vegetation monitoring,
151 early warning systems and other (Brust et al., 2019; Hoeser & Kuenzer, 2020; Miyamoto et al., 2018; Redmon et al.,
152 2016; Szegedy et al., 2013; Y. Wu et al., 2019a, 2020; Zhao et al., 2019).

153 In the last two decades a lot of efforts have been made to use Deep Learning to solve planetary mapping problems on
154 Earth (Liu et al., 2004; Paul & Ganju, 2021; Stepinski et al., 2007; Talukdar et al., 2020) as like as on Mars (Hipperson
155 et al., 2020; Nagle-McNaughton et al., 2020; Palafox et al., 2017; Wilhelm et al., 2020) and the Moon (Hu et al., 2021;
156 Silburt et al., 2019; S. Wang et al., 2020) exploring almost all architectures and algorithms with very promising results.
157 In some cases the code used for the analysis is publicly available (Aye et al., 2019; Barrett et al., 2022; Lee, 2019;
158 Silburt, 2017/2019; Wilhelm et al., 2020) and may be used to create preliminary map products.

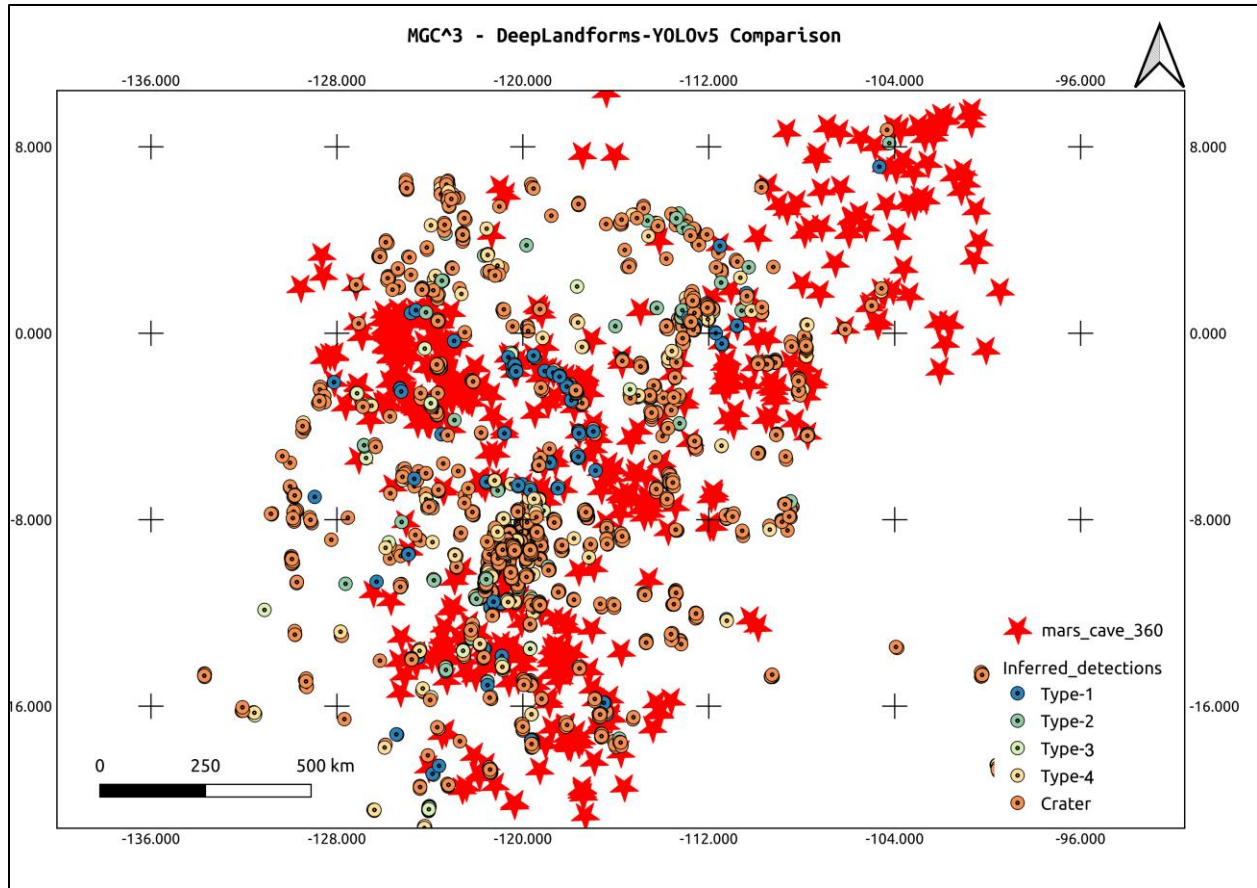
159 The results obtained with the above-mentioned codes are typically plain images with superimposed the bounding
160 boxes or the segmented area and are in non-georeferenced raster file type formats such as png or jpeg. Those type of
161 results need to be georeferenced before being further processed in GIS software to vectorize manually all the objects
162 or segments and finally obtain a vectorial map that can be published in a geospatial data format such as OGC
163 Geopackage. This newer file format is specific for transferring geospatial information similarly to ESRI shapefiles
164 (ESRI technical document, 1998), but with higher portability and compactness, moreover is an open format and
165 standard-based (Open Geospatial Consortium, 2021).

166 For instance, segmented areas such those that represent geomorphological units, need to be manually digitized as
167 individual shapes in GIS software, with the manual conversion and assignment of the properties of the units in the
168 image.

169 In this setting, geologists and geomorphologists, not familiar with programming languages and interested only in
170 workflows and tools may have a lot of difficulties understanding and using complex machine learning approaches that
171 require higher knowledge in computer science, especially if complete and ready-to-use tools are not available.

172 In this work is presented a first complete working release of *DeepLandforms*, a set of comprehensive and ready-to-
173 use tools specifically developed for planetary mapping.

174 This toolset is a follow-up of the work and tool (Nodjoumi et al., 2021) based on object detection methodology and
175 focused on the usage of You Only Look Once version 5 (YOLOv5) framework (Pham et al., 2020; *Ultralytics/Yolov5*,
176 2020/2021) to detect sinkhole-like landforms on Mars, obtaining a geopackage containing, the centroid coordinates
177 of the bounding boxes, confidence level and classification class for each of the detections. In Figure 2 the map showing
178 both the MGC³ catalog and the object detection results.



179

Figure 2. Comparison of MGC³ catalog and results obtained by using Deep Learning object detection (DeepLandforms-YOLOv5) on a similar dataset (Nodjoumi et al., 2021).

180

181 Despite centroid coordinates could be considered a starting point for proper mapping, there is the lack of the spatial
 182 dimensionality thus providing only a general localization of the features, even using the coordinates of the detection
 183 boxes there is still the lack of a precise localization and definition of the shapes of the landforms. To further improve
 184 the previous work, a change of architecture was mandatory, moving from object detection to instance segmentation
 185 architecture.

186 The instance segmentation library selected for this work is the Detectron2 Library, developed and periodically
 187 maintained by the Facebook AI Research team, specialized in image segmentation tasks through R-CNN networks.
 188 See supporting information Text S2 for additional details on Detectron2 Library.

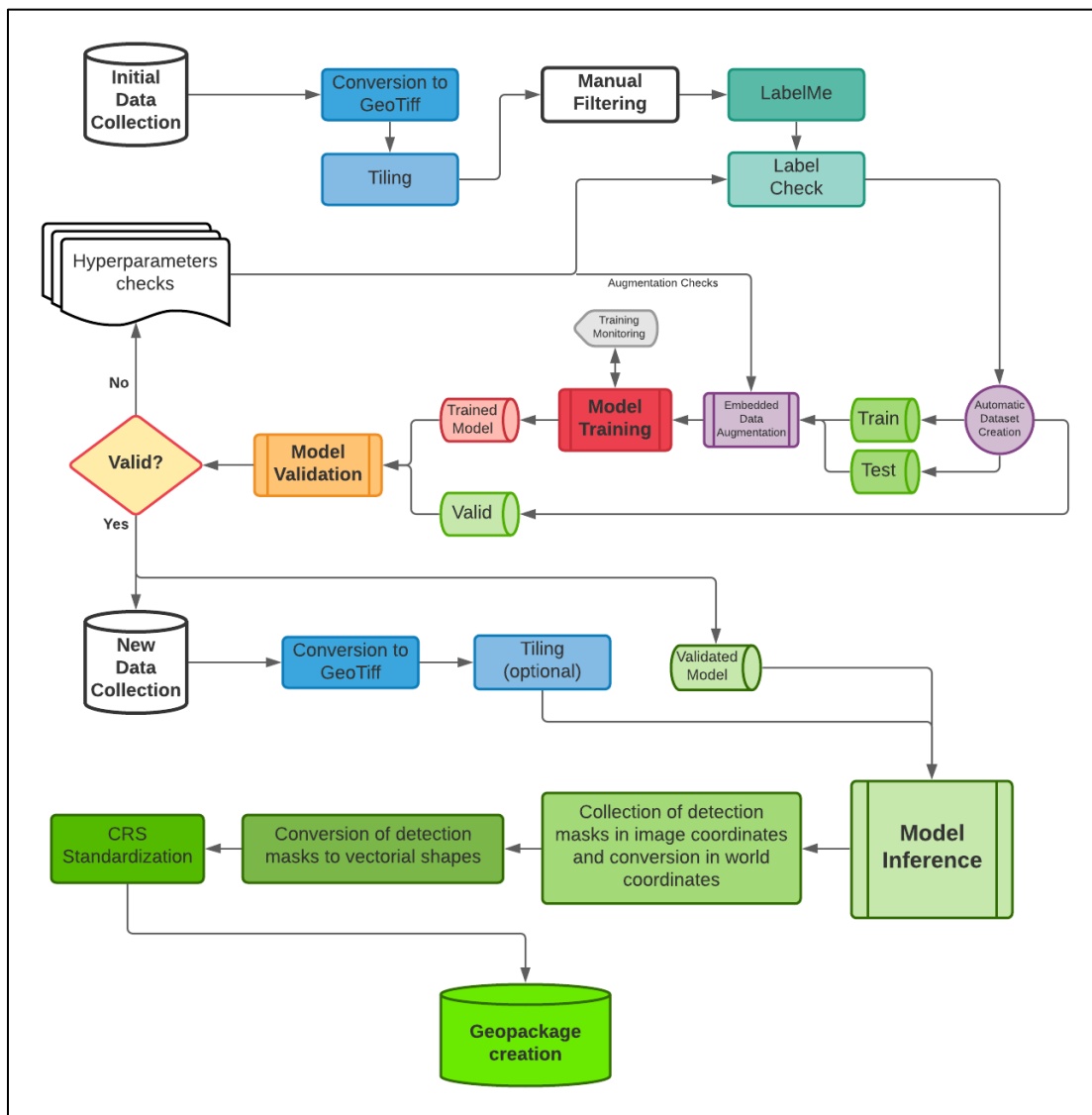
189 In this work, the Mask R-CNN network has been considered the only main network since it is specific for object
 190 instance segmentation tasks (He et al., 2018).

191 Mask R-CNN extends Faster R-CNN, class labels and bounding boxes, by adding a third output, the objects masks
 192 (He et al., 2018; Massa & Girshick, 2018). A mask can be considered as a method of describing an image in boolean-
 193 based representation by using specific filters or functions, meaning that the content of the image will be converted in

194 only two possible values (0-1, on-off, true-false, and so on). See supporting information Text S5 and Figure S1. Each
 195 mask is then characterized by internal and external values and can be localized by using image pixel coordinates.
 196

197 2. DeepLandforms

198 *DeepLandforms* has been developed with the aim of creating a comprehensive set of tools to support a complete
 199 workflow for mapping landforms using georeferenced data and producing results in vectorial format. Flowchart of the
 200 workflow can be visualized in Figure 3.



201 **Figure 3.** Flowchart of the complete workflow on which is based the DeepLandforms toolset.
 202

203 The toolset is composed by four major components, all based on docker open platform (*Docker Overview*, 2021;
 204 Merkel, 2014), which is a state of the art, well-known, open-source platform for developing, sharing and running

205 applications as a sandbox service called *containers*, with full support for NVIDIA GPU (CUDA) computing (Luebke,
206 2008). More information on docker available on supporting information Text S5.

207 The first component is the *ImageProcessingUtils* docker container (Nodjoumi, 2021a), a jupyter notebook tool
208 developed for resize, crop, remove black borders, tile and convert images from CUB (Anderson Jeff & Deborah Lee
209 Soltesz, 2003), jpeg2000 and GeoTiff file formats to GeoTiff, jpeg and png file formats maintain georeferencing
210 information in file metadata for GeoTiff or in an ancillary world files for jpeg and png.

211 The second component, is *Labelme* docker container, an open-source tool with graphical user interface for creating
212 segmentation labels (Wada, 2021).

213 The third component is DeepLandforms docker container which includes two jupyter notebook, both built on top of
214 Detectron2 library, *DeepLandforms-Training* and *DeepLandforms-Segmentation*. More detailed description are
215 provided in supporting information Text S6.

216 The fourth component is *Tensorboard* docker container, a simple utility for monitoring the training process.

217 3. Materials and Methods

218 3.1. Data

219 The data used in this work are mainly images acquired by image sensors operating in the visible (VIS) and Near
220 InfraRed (NIR) spectrums on board of probes orbiting Mars and the Moon as shown in Table 1.

221

Orbiter	Target	Instrument	Sensor type	Ground Resolution	Images
Mars Reconnaissance Orbiter (MRO)	Mars	High Resolution Image Science Experiment (HiRISE)	Panchromatic VIS+NIR	Up to .30 m/pixel	~1000

222 **Table 1.** The dataset used for training and testing purposes is a combination of three subset samples of global coverage
223 major datasets.

224 This dataset is composed of images by different instruments and space missions downloaded both as Reduced Data
225 Record (RDR) and Experiment Data Record (EDR) format from public space archives such as PDS Geosciences Node
226 Orbital Data Explorer (ODE) (PDS Geosciences Nodes, 2021). EDR images have been processed initially to produce
227 RDR version using USGS Integrated Software for Imagers and Spectrometers (ISIS) (Laura et al., 2021) and then
228 converted into jpeg2000 (JP2) file format or GeoTiff file format using *ImageProcessingUtils* container.

229 Computational requirements of Machine Learning and more in particular of Deep Learning architectures for Computer
230 Vision, apart from the complexity of the architecture, are strictly related to image properties, image bands, resolution
231 (size), dataset size, that have a great impact especially during training of the model. On the other hand, the impact on
232 computation and resources during the usage of the pre-trained model is lower. In comparison, the Mars and Moon
233 high-resolution images from HiRISE and LROC respectively, are enormous in terms of data size, reaching easily
234 50000pixel height resolution at 0.3m/pixel ground resolution (on average). These require a lot more processing in
235 order to make them compatible with Deep Learning tasks or to reduce the computational requirements.

236 A simple and easy approach would be the direct resize of these images but is not always possible because there is the
237 risk of loose object's unique details or even worse introduce apparent similarity between two different objects.

238 A better approach is to divide the images into desired resolution tiles, in this case there is no detail loss but the number
239 of images to be filtered out of irrelevant ones and then labeled increases proportionally of image original and desired
240 resolution. E.g., HiRISE PSP_004715_1855_RED image is 30137x76047 pixels, dividing it into ~512x512 pixels
241 tiles results in more than ~8700 tiles. Even tiling into larger tiles is not always a feasible approach. Moreover, such
242 tiling may result in the loss of contextuality of the objects or introduce difficulties during the labeling tasks since the
243 object may result splitted into multiple tiles.

244 In this situation it is advised to define the requirements of the analysis and evaluate compromises between the
245 approaches of Table 2.

Requirements	Limits	Compromises	Approach
Maintain context	Scaling to very low resolution may lead to huge loss of details	Limit the scaling to maintain discretization capabilities	Scaling approach
Maintain high discretization and avoid object splitting	Larger images produce several tiles proportional to original image and tiles resolution, objects may results split across several tiles	Limit the dimension of the tiles to avoid object splitting and number of tiles low	Tiling approach

246 **Table 2.** Comparison between approaches, scaling approach may be better for analysis of features at regional scale,
247 while tilin approach may be preferred for smaller landforms.
248

249 In the presented use case, a mixed approach has been used: images spatial resolution have been scaled down to 5
250 m/pixel, then the resulting images have been sliced into tiles with 1024 pixel max width or height. To achieve these
251 specific tasks, the docker container named ImageProcessingUtils.

252 3.2. Masks world coordinates

253 As mentioned in the introduction, all results obtained by Mask-R-CNN are image masks described with pixel
254 coordinates. Therefore it is necessary to convert in world coordinates. This operation has been accomplished by
255 developing a function based on a Python library named Rasterio (Gillies & others, 2021) which contains specific
256 modules for spatial data manipulation by using each image affine transform. See Text S4 and Figure S1 in supporting
257 information.

258 4. Results

259 Hereby are described the results obtained after re-training Mask-R-CNN models on a custom dataset of HiRISE
260 images containing pit/skylights landforms.

261 All the configuration parameters, the components of DeepLandforms, including the descriptions of the data pre-
262 processing and labeling components, the training and inference jupyter notebooks and the types of results obtainable
263 are available in supporting information Text S3, S4, S5, S6, S7, Table S3, S4, S5.

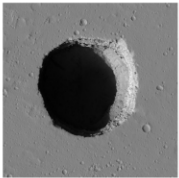
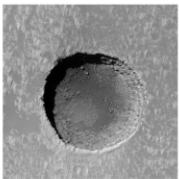
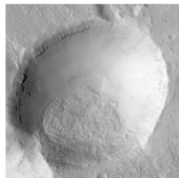
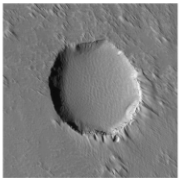
264 4.1. Pits/Skylight use-case

265 Despite this toolset is not specific to any kind of landforms, the target used as test landform consist of pits/skylights
266 with a comparison with craters.

267 Craters are almost circular to elongated depressions caused by an impact of an object. Dimensions may vary a lot
268 across the solar system and are guided by several aspects such as the presence of an atmosphere, the geology of the
269 area, the velocity and trajectory of the object, the gravity of the planet and more. Commonly, they are characterized
270 by a bulged rim, shallow to steep walls, radial eject marks and a small summit at the center (Evans, 2012; Hargitai &
271 Kereszturi, 2015b; Michikami et al., 2014; Mouginiis-Mark, 2004). These characteristics are more visible in craters
272 that are newer, larger, or more in general, that were less subject to recent or present erosional processes, e.g.
273 atmospheric ones in the case of Mars. In later stages of erosion and alteration some characteristics tend to be obliterated
274 or smoothed, resulting in morphologies that resemble pits or skylights.

275 Pit and skylight are depressions of the terrain characterized by an elongated to almost circular shape, flat rims and
276 bottom, walls ranging from almost flat to very steep and in some cases sub-vertical (Cushing et al., 2015; Cushing &
277 Titus, 2010; F. Sauro et al., 2020; U. Sauro, 2016; van der Bogert & Ashley, 2015; Wyrick, 2004). On Earth are
278 commonly caused by the collapse of the top of a subsurface cavity, or by chemical or mechanical erosion of the
279 subsurface sediments, while on other planetary bodies such Mars and the Moon, their formation mechanisms are still
280 debated. As mentioned before, pits and skylights may have different shapes and dimensions on Earth and other
281 planetary bodies (Cushing et al., 2015; Hong et al., 2015; F. Sauro et al., 2020; Sharma & Srivastava, 2021; Whitten
282 & Martin, 2019), yet maintain almost all the characteristics. The classification proposed Figure 4, is an expansion of
283 the classification proposed by Cushing et al (Cushing et al., 2015) and is based only on a qualitative morphological
284 analysis based on visual appearances of the features characteristic of pits and skylight, without taking into account
285 morphometric properties.

286

Image	ID	Description
	1a	Type 1a – Skylight with possible cave entrance characterized by quasi perfect circular shape, flat rim, no ejecta marks, and almost nonvisible bottom. When visible bottom is present, it is possible to see vertical to overhanging walls by the projected shadows and in some cases piles of debris at the center with conical upward shape. Often found isolated or in proximity of all other types, especially Type-4 and Types-2a-b.
	1a	Type 1b – Pit with possible relation to cave entrance and, or lava tube characterized by quasi circular shape, sub-vertical to vertical walls, almost flat rim, no ejecta marks, almost circular shape, and visible bottom. In some cases, it is possible to see circular marks of darker terrain on the floor, near the sub-vertical walls.
	2a	Type 2a – “Bowl” pit with uncertain connection to lava tubes or dikes characterized by a semicircular shape, almost flat rim, no ejecta marks, sloped walls and visible convex bottom. Often isolated or in connection with Type-3
	2b	Type 2b – Pit with uncertain connection to lava tubes or dikes characterized by a semi elliptic shape, almost flat rim, no ejecta marks, sloped walls and visible convex to flat bottom. Often isolated or in connection with Type-3
	3	Type 3 – Coalescent pits characterized by a mix of characteristics of Type-2a-b. Possible connection to lava tubes or dykes due to the alignment of Type-2a-b.
	4	Type 4 – Pit with possible connection to lava tubes or dikes due to the alignment of multiple similar shapes, characterized by a semicircular shape, almost flat rim, no ejecta marks, shallow to very shallow depth, sloped to sub-vertical walls and visible flat bottom. Often aligned with other Type-4 or in connection with Type-3 and Type-1a-b, rarely isolated.

287

Figure 4. Main types of pits/skylights that can be identified on Mars, also used as classes for labeling training dataset, expanded from a previous work (Nodjoumi et al., 2021).

288 The most consistent and peculiar characteristic among pits/skylights that almost always differ greatly from craters is
 289 the presence of a raised rim. As previously mentioned, in craters it’s common to find bulge all along the rim, or in a
 290 specific direction that usually correspond to the impact trajectory, while rims in pits and skylights are almost

291 completely absent or associated with previously existent landforms that can be visible also in the nearby of the pits
292 and skylights.

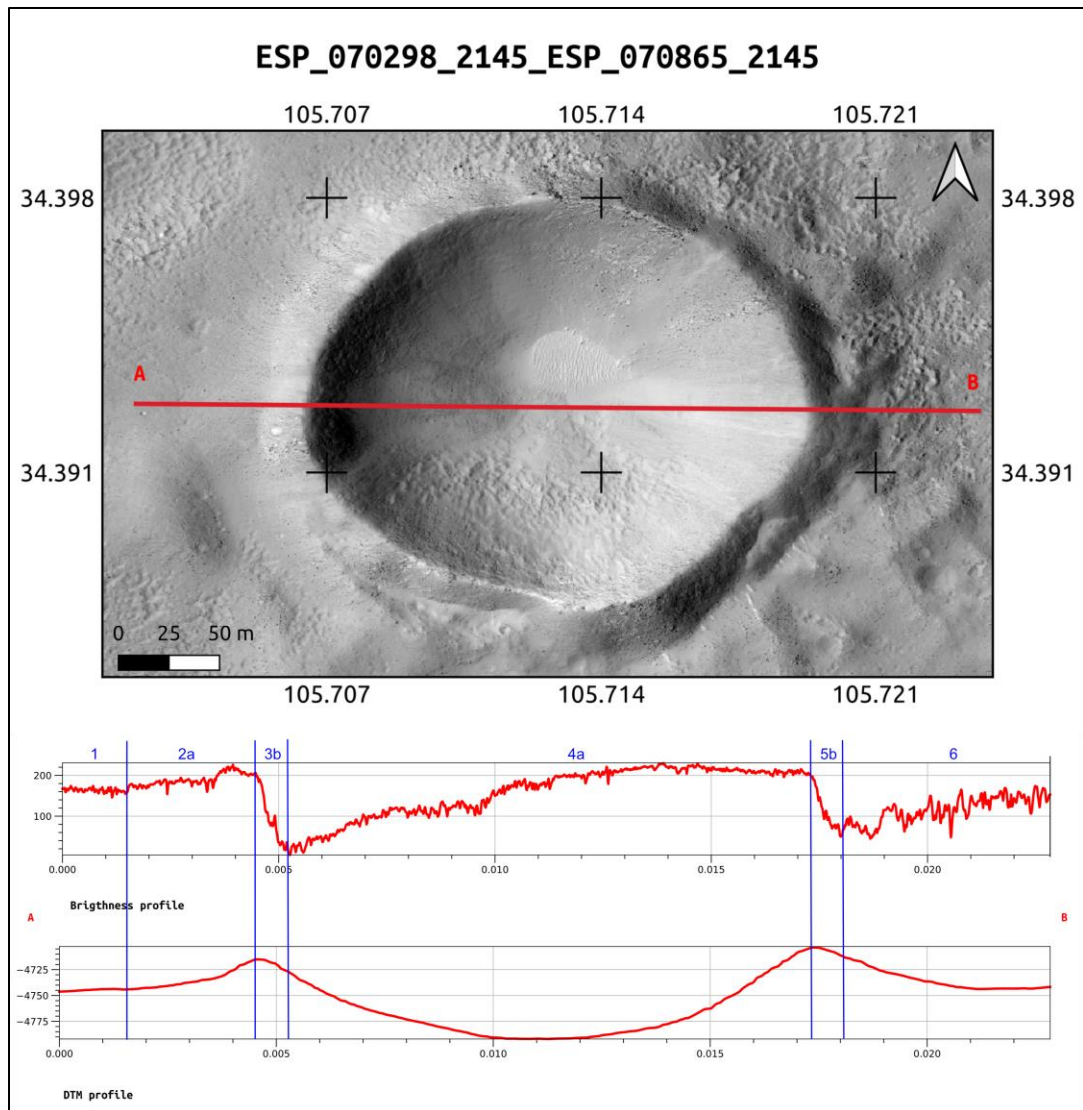
293 The best method to evaluate the differences between pit and crater rims, is to manually plot and evaluate Digital
294 Terrain Model (DTM) profiles but, since in most cases DTMs are not always available, it is possible to evaluate them
295 by plotting a profile along the maximum illumination direction of visible images, obtaining a pixel intensity profile
296 that correspond to brightness levels of the pixels, with digital number (DN) with values ranging from 0 (black) and
297 255 (white). Although 16-bit images could provide major details in the shadowed areas, 8-bit images were preferred
298 as their 16-bit counterpart increases computational requirements dramatically and are not completely implemented yet
299 in common Deep Learning techniques for object detection and segmentation. This method is an approximated and
300 indirect estimation of the orientation of the surface and assumes that the substrate is almost homogeneous. Low
301 brightness values correspond to shadowed areas with solar incidence angle near 90° , while high brightness values
302 correspond to lower solar incidence angle. The solar incidence angle is the angle between the solar rays and the normal
303 on a surface and has an absolute range between 0° and 90° (Kalogirou, 2009). This approach is also the core of other
304 works that have the same aim of identifying pits on other Solar System rocky bodies (Lohse et al., 2006; Robinson et
305 al., 2017).

306 Craters brightness profiles can be created using QGIS profile plugin as shown in Figure 5.

307 Profiles can be divided in six main sections, in which there are almost two pairs of paired high peak-bottom brightness
308 sections corresponding to the area of morphological bulge's illuminated and shadowed faces. Those sections can be
309 described as follows:

- 310 1) Pre-rim: brightness is almost uniform and visually similar to the surroundings of the landform.
- 311 2) 1st Sun-faced rim: inner side of the pit exposed to direct sun's rays opposite of section 2. Divided in two sub-
312 sections:
 - 313 a. Lower ramp: brightness increases gradually towards the rim with values up to those of section 1. Not
314 always present in conjunction with 3b.
 - 315 b. Higher ramp: brightness increases abruptly, with values equal or major than those of section 1, meaning
316 that the solar incidence angle is decreasing. Not always present in conjunction with 3a.
- 317 3) 1st anti-solar rim: side of 1st bulge not exposed directly to sunlight, brightness decreases with values lower
318 than section 1, depending on inclination of the internal bulge and the landforms. Divided in two subsections:
 - 319 a. Penumbra: brightness decreases uniformly. Non always present in conjunction with 3b.
 - 320 b. Umbra: brightness decreases abruptly, usually completely dark or with DN values near to 0, those values
321 may slightly increase moving near the next rim or increase abruptly. Non always present in conjunction
322 with 3a.
- 323 4) 2nd sun-faced rim: side of the 2nd bulge, divided in 4a and 4b, similarly to section 2a and 2b.
- 324 5) 2nd anti-solar rim: side of the 2nd bulge, divided in 5a and 5b, similarly to section 3a and 3b.

325 Post-bulge area: brightness increases up to levels similar to section 1.



326

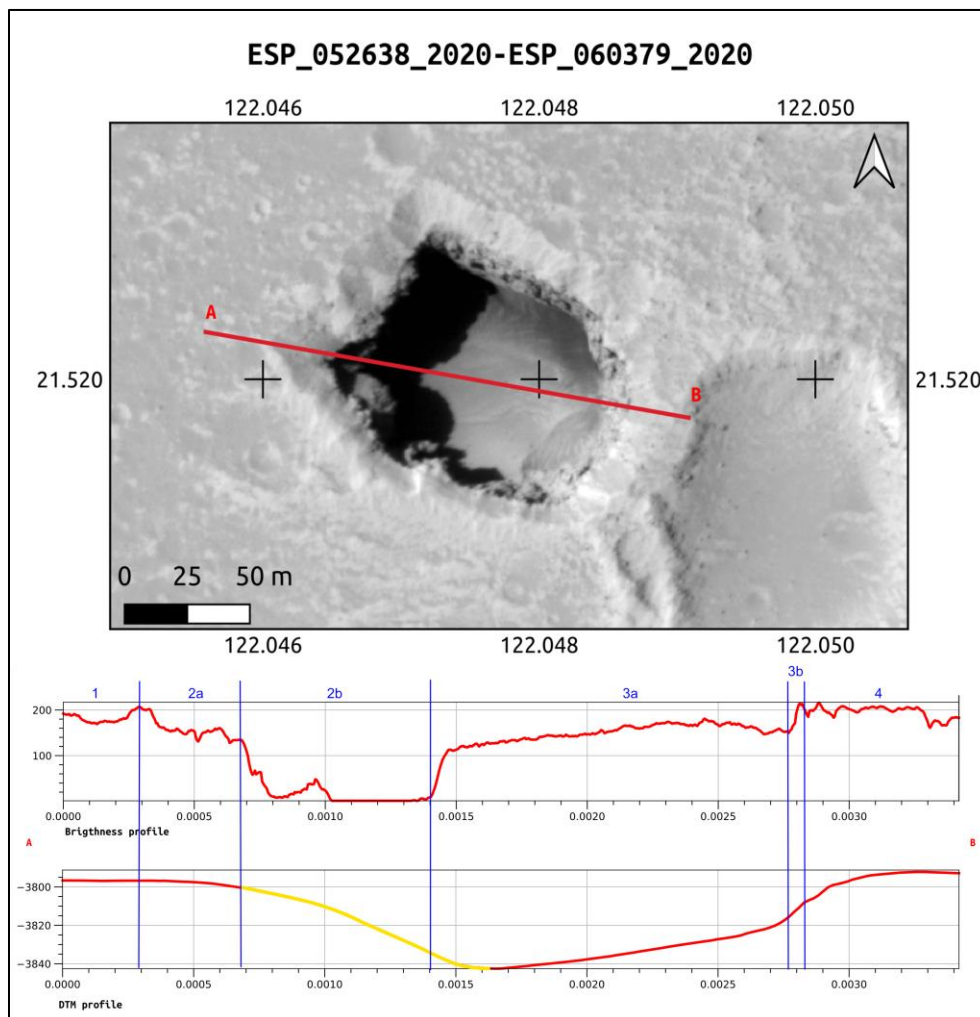
Figure 5. Comparison of brightness and DTM profiles for a crater on ESP_070298-ESP_070865 stereo pair, red channel. In blue, an attempt to identify the correspondence of the brightness sections on a DTM derived from photogrammetry of HiRISE stereo pair.

327 Pits/Skylights brightness profiles, created using QGIS profile plugin, as shown in Figure 6. Additional example in
 328 Figure S3 in supporting information.

329 The profiles are divided in 4 main sections, described as follows:

- 330 1) Pre-pit: brightness is almost uniform with values similar to the surroundings of the landform.
- 331 2) Funnel: brightness decreases with values lower than section 1, depending on inclination of the morphological
 332 slope of the surfaces. Divided in two sub-sections:
- 333 a) Penumbra: brightness decreases uniformly. In some cases, brightness may drop abruptly then remaining
 334 almost constant or decreasing uniformly with values always higher than DN 0. Non always present in
 335 conjunction with 2b.

- 336 b) Umbra: brightness decreases abruptly, usually completely dark or with DN values near to 0, those values
 337 may slightly increase moving near the next rim or increase abruptly. Non always present in conjunction
 338 with 2a.
- 339 3) Sun-faced rim: inner side of the pit exposed to direct sun's rays opposite of section 2. Divided in two sub-
 340 sections:
- 341 a) Lower ramp: brightness increases gradually towards the rim with values up to those of section 1. Not
 342 always present in conjunction with 3b.
- 343 b) Higher ramp: brightness increases abruptly, with values equal or major than those of section 1, meaning
 344 that the solar incidence angle is decreasing. Not always present in conjunction with 3a.
- 345 4) Post-pit area: intensity levels become similar or identical to those of section 1.



346 **Figure 6.** Comparison of brightness and DTM profiles for a Type-1 on ESP_052638_2020-ESP_060379_2020 stereo
 347 pair, red channel. In blue, an attempt to identify the correspondence of the brightness sections on a DTM derived from
 348 photogrammetry of HiRISE stereo pair. In yellow, the portion of the DTM profile interpolated by the Socet Set ((c)
 349 BAE Systems) software. The interpolation is due to lack of usable data in both the images processed using
 350 photogrammetry (HiRISE | About HiRISE Digital Terrain Models, 2021).
 351

352 In order to validate all the packages, tools and the complete workflow, an intensive test has been performed on the
353 above-mentioned pit, skylights landforms, including a generic set of craters for references and for testing the capability
354 to discriminate those whose appearance resemble some types of pits.

355 The dataset consists of 89 HiRISE RDR red channel images, see supporting information Table S5. The use of only
356 red channel images is due to the swath of 6 km cross-orbit and 20 km along-orbit at a nominal 300 km nominal orbit.
357 In comparison the Blue-Green and NIR images have a swath resolution of 1.2 km cross-orbit.

358 Those image have been processed using ImageProcessingUtils (Nodjoumi, 2021a) to convert from jpeg2000 file
359 format (JP2) to GeoTiff and then resized to a common 5 m/pixel cell size, and tiled into more usable files with the
360 largest side up to maximum 1024 pixel.

361 All resulting images have been manually examined to filter out those which did not contain any landform relevant for
362 the labeling steps, obtaining 152 images containing at least one type of landform.

363 Then, all the images have been ingested into LabelMe to annotate all the pits, the skylights and some representative
364 craters following the classification showed in Figure 4. At the end of the labeling task, it emerged that the obtained
365 labels were unbalanced, meaning that the dataset does not contain an almost equal number of each class.

366 Since the collection and processing of newer images containing more landforms of the unbalanced classes was not
367 feasible at the time of analysis, a simpler approach was chosen and consist of a reduction of the classes by grouping
368 into similar ones, doing so resulted in only four classes, Type-1, containing -1a and -1b, Type-2, containing -2a and -
369 2b, Type-3, Type-4.

370 After concluding the dataset preparation, several training sessions were performed using DeepLandforms-training
371 notebook, with different parameters and *mask_rcnn_R_50_FPN_3x* as model configuration; to evaluate the stability
372 and scalability and the performance of the tool with the dataset on two different computers.

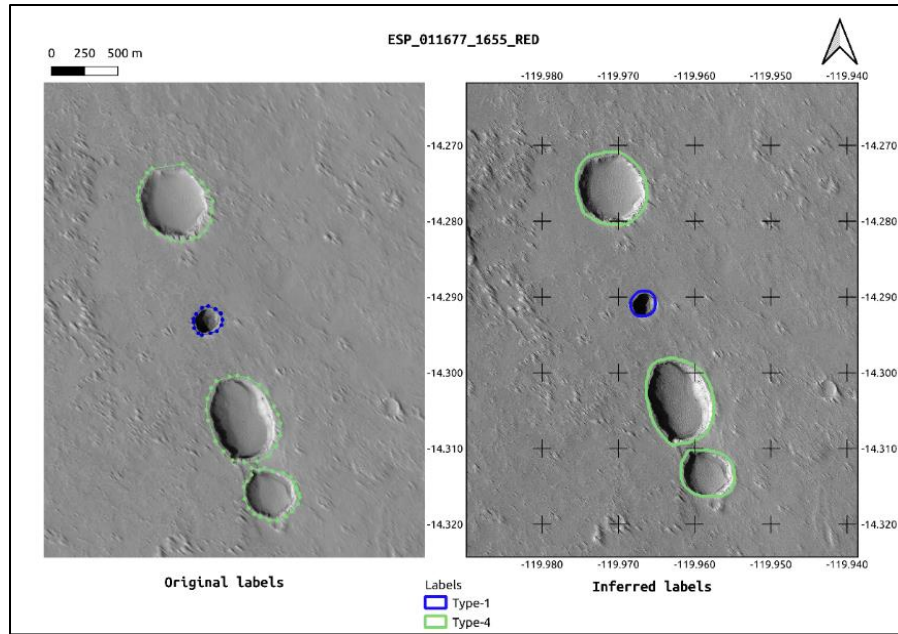
373 According to Detectron2's model zoo (Y. Wu et al., 2019b), which is a large collection of model configurations and
374 their corresponding pre-trained models and baseline performance values, *mask_rcnn_R_50_FPN_3x* model
375 configuration is reported to have the best-balanced results/training requirements ratio, see supporting information Text
376 S7 for details on the model configuration. The ranges of the main training parameters are summarized in supporting
377 information Table S3.

378 All the training sessions have been monitored using tensorboard to evaluate the progression and the performance of
379 the trainings and resulted in promising results, despite the small dimensions of the datasets and the not optimized
380 training parameters. As it is possible to see in supporting information Figure S11, the accuracy for bounding boxes
381 and masks reached more than 0.99 after 5000 epochs, with very low ratios of false negatives and false positives and
382 final mean Average Precision values shown in supporting information Table S4 and Figure S9-S10.

383 Those values are mostly in accordance with the average values of the architecture's benchmarks (Y. Wu et al., 2019b),
384 the low values obtained for craters and Type-4 are mainly caused by the low quantities of respective labeled data and
385 the similarities that may occur in some landforms.

386 The obtained model was then used to inference the valid dataset, and then the results were loaded into LabelMe to
387 check if the labeled objects are detected and labeled correctly as shown in Figure 7.

388



389
 390 **Figure 7.** Comparison between ground truth labeled image used in training (left) and inferred labeled image (right).
 391 The major difference is in the density of the points of the shape, where in the inferred image are way denser than those
 392 of the ground truth.

393 Then the model was used on a partially new set of HiRISE RDR red channel images, in a limited area over the Tharsis
 394 Region on Mars.

395 This region has its central coordinates at $0^{\circ}\text{N } 260^{\circ}\text{E}$ and was selected three of the largest shield volcanoes in the Solar
 396 System are located here, Arsia Mons, Pavonis Mons and Ascreus Mons, moreover in its western area is located the
 397 tallest shield volcano in the Solar System, the Olympus Mons. Considering the presence of these large shield volcanoes
 398 this region and thus possible intact lava tubes, is the best candidate region to look for possible cave entrances. A
 399 previous work by Cushing et al. (Cushing, 2017), identified and published a database containing thousands of
 400 pit/skylights landforms, by analyzing manually several Context Camera (CTX) and HiRISE imagery.

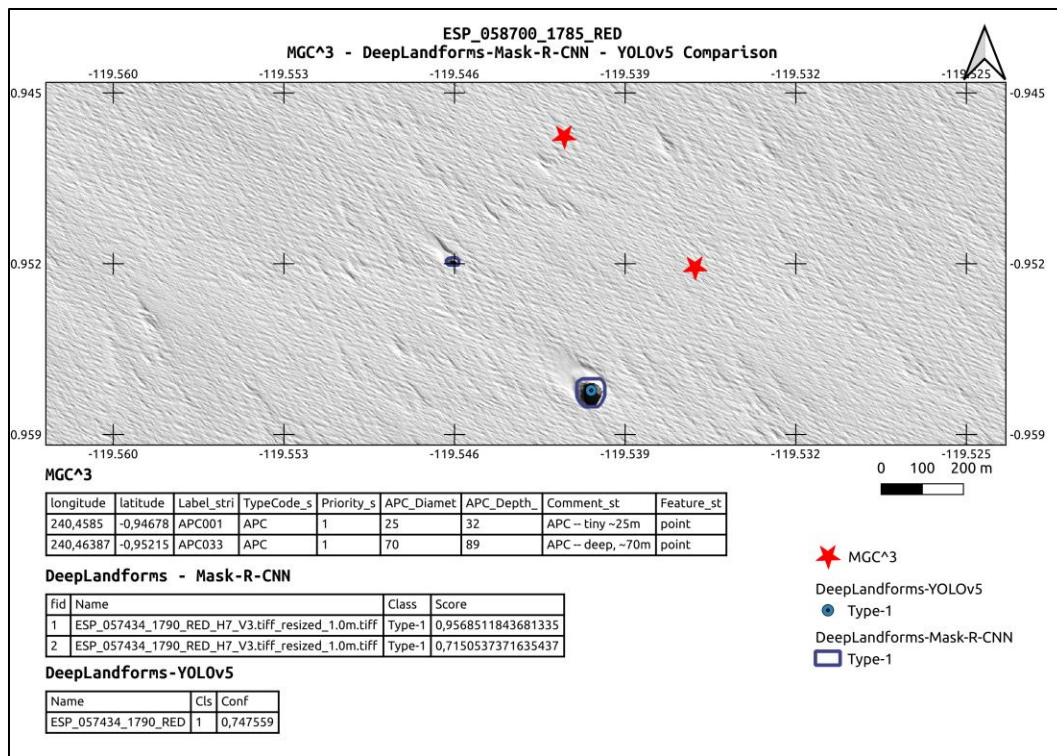
401 This database was used as a control data for all the analyses performed in this and the previous work (Nodjoumi et al.,
 402 2021).

403 The results of the inference performed using DeepLandforms, contained in a geopackage file, was imported in QGIS
 404 software, to better inspect the results obtained as shown in Figure 8.

405 It is possible to see multiple mis-aligned detections of the same landform, this is not properly an error since and is due
 406 to presence of two images that are originally acquired from different orbit and not perfectly coregistered or granules
 407 relatives to a stereo pair, thus the slightly misalignment, which does not affect the manual validation. To avoid these
 408 occurrences, it is necessary to manually check the working dataset for duplicates or use only coregistered data.

409 In Figure 8, is presented an example of the obtained results, compared to the entries of the MGC³ database and
 410 the results obtained in the DeepLandforms-YOLOv5 object detection work, showing a very good detection and
 411 segmentation of the trained landforms. Moreover, it is possible to see the advantages of the approach proposed in this
 412 work. Providing polygon geometries as results, could greatly improve the mapping of specific landforms, especially

413 when looking for unknown occurrences on a wide dataset. More examples are available in Supporting information
 414 Figures S4 to S8.
 415



416
 417 **Figure 8.** Example of detection on HiRISE Red channel image and comparison between MGC^3, DeepLandforms-
 418 YOLOv5 object detection and DeepLandforms-Mask-R-CNN instance segmentation. Tables show attributes of fields
 419 in the shapefiles. The offset of MGC^3 points is probably caused by the coordinate conversion of the source MGC^3
 420 csv file into shapefile.

421 Notice that in all the presented images, there is a misalignment between the MGC^3 points and the HiRISE or CTX
 422 Images. The cause of this discrepancy has not been identified yet but is probably due to a different reference system
 423 used by the authors of MGC^3 or introduced during the conversion from the source MGC^3 csv file to the shapefile
 424 file format.

425 5. Discussion

426 In this work, are presented the mapping results of skylight, pit and pit chains automated mapping using only
 427 DeepLandforms, a novel comprehensive toolset based on Deep Learning Computer Vision for object detection and
 428 segmentation.

429 Skylight, pits and pit chains are an extremely interesting type of landforms that can be observed on almost all rocky
 430 planets and moons of the Solar System.

431 Formation mechanisms are commonly related to volcanic and tectonic processes but are still debated, moreover it is
 432 still not clear whether such formation mechanisms are the same on all the planetary bodies in which those landforms

433 are observed, especially since there are very similar and common morphological characteristics among all
434 observations. If it is the case of common formation mechanisms, this implies that there should be shared geological
435 properties and settings among those bodies, thus common geological history.

436 Further on, skylights and some pits may have access to caves as observed on Earth analogues, and hypothesized on
437 Mars and the Moon (Hong et al., 2015), such those found on large shield volcanoes (Léveillé & Datta, 2010; F. Sauro
438 et al., 2020). Presence of accessible caves on other planets and moons has an huge importance for space exploration
439 since those cave may contain traces of life, both past and potentially present, as some extremophile bacteria and other
440 smaller life-form may have found shelter from harsh surface condition and cosmic radiations (NASA, 2021).
441 Moreover, caves are considered as good candidates for future human habitation outposts (Cushing & Titus, 2010;
442 Pipan & Culver, 2019), and also are an excellent window on the subsurface structure, thus providing valuable
443 information for understanding the geological settings and evolution of the area and potential direct access to mineral
444 resources (Blamont, 2014).

445 To explore the above-mentioned targets and objectives, is necessary an accurate and global scale mapping of skylight,
446 pit and pit chains, in order to better understand the spatial distribution of such landforms and correlate their presence
447 with other geological and non-geological features and settings.

448 For instance, since pit chains may be related to the presence of lava tubes or dykes (Ferrill et al., 2011; Whitten &
449 Martin, 2019; Wyrick, 2004), mapping pits could lead to new understandings of lava tube distribution, thus to better
450 knowledge of volcanic processes involved, even across planets and moons. Isolated pits with no surrounding other
451 morphological evidence may indicate the presence of a deep buried lava tube or cavity originating from other
452 processes.

453 It is also possible to compare the distribution of such landforms with structural maps or other features that may be
454 interconnected (Ferrill et al., 2004, 2011).

455 Another advantage is connected to the planetary human mission planning, since the availability of geomorphological
456 maps, even if not at highest resolution possible, may lead to the identification of better scientific targets or path
457 planning in case of rovers.

458 An automated or semi-automated approach as the one proposed in this work, in comparison to the manual mapping,
459 may be a game-changer, providing robust processing workflows for generate high-end data in compliance with the
460 OGC standards, for map productions at planetary scale, with the enormous advantage of relaying the most time-
461 consuming task of data pre-process and first analysis to computer time instead of human-time.

462 Presented results are very promising, despite some issues that must be considered.

463 Despite the very good correspondence of the shapes of the detections and the proper real shape, some refinements
464 may be necessary, as some landforms are not detected at all, or in some cases wrongly classified.

465 Moreover, in some cases there is a detection ambiguity, in which some resulting shapes appear doubled, non-unique
466 or mis-aligned, due to the analysis performed on not co-registered images of the same area, as shown in Figures S4
467 and S8 in supporting information.

468 Poor labeling and bad train configuration parameters can also lead to models not suitable for deployment in production
469 uses, or completely unreliable.

470 To improve those results the first step is to increase the quality and quantity of the training dataset, then tuning the
 471 configurations of the architecture used and eventually try different networks that may be more adequate to different
 472 landforms.

473 The analysis presented in this work, if expanded to a large dataset, may greatly expand the knowledge of the spatial
 474 distribution of skylights, pits, and pit chains, including those already known and described, providing a detailed wide
 475 map that can be further integrated with morphometric analyses.

476 All the main blocks of the workflow presented in Figure 3 were performed exclusively on DeepLandforms's modules,
 477 data collection was performed using NASA-PDS data archive web services, and results evaluation and comparison
 478 was performed using QGIS software.

479 The quality of the obtained results can be improved by increasing the amount of images in the initial dataset and their
 480 spatial resolution. This will provide more labels to the model that will better learn the differences among all the studied
 481 objects. Hyperparameters of the used network can be also tuned to achieve better results. This applies not only to this
 482 specific case but to every object detection and segmentation problem.

483 The major limit of those automated approaches resides in the context-unawareness, meaning that when performing
 484 the analyses, all the networks are not performing a context-aware analysis in addition to the object detection and
 485 identification. This means that at the time of writing there are not yet architectures, for this kind of tasks, that evaluate
 486 the surrounding, the context, of a detection to optimize the identification of the objects present in the area.

487 Recently there are architectures that are capable of such additional analyses, called *Liquid Time-constant Networks*
 488 (Hasani et al., 2020) but are still under development.

489 6. Conclusions

490 The advantages and improvements in data analysis provided by machine learning are undoubtful and constantly
 491 expanding in more and more sectors especially in remote sensing of Earth and Space. With an exponential amount of
 492 fast-growing available datasets, newer and faster methods are necessary to perform a continuous stream of analyses,
 493 and with a plethora of publications, works, architectures and unconnected tools available, that are mainly *accessible*
 494 by everyone, albeit not *usable* by not insiders, is also necessary to make those available for the wider audience,
 495 especially those who are involved in the analyses of data but are not specialized in the machine learning.

496 In these settings, DeepLandforms, presented in this work, may be a forerunner, a tentative to lead an easier approach
 497 well suitable both for first-time users and advanced users.

498 The major advantages and disadvantages are summarized in Table 3:

Advantages	Disadvantages
Almost ready-to-use	Not compatible to every platform
Semi-automated approach	Require intensive user supervision in the initial phase and during preliminary evaluation
Large data volume processing capabilities	Depends on the machine in which is running
Possibly to use results for further correlation with other data	
Wide adaptability to different landforms	May not be compatible with every landform type, depending on the training data

499 **Table 3.** Tabulated assets and liabilities of the toolset presented in this work.

500 6.1. Further development

501 Further development includes implementation of sliding window to improve further the segmentation of large images
502 without pre-tiling them, the integration with GIS statistics such as the parametrization of the detected shapes, including
503 cross-analysis of different data types such as Digital Terrain Models (DTM) in order to improve the quality of the
504 results including eventually volume estimation, or integration with hyperspectral data to retrieve a mineral
505 composition of the surface.

506 Another development could integrate the workflow with the shape-from-shading technique (Alexandrov & Beyer,
507 2018; Lohse et al., 2006; Micheletti et al., 2015) in order to extract depth and thus volume information where DTMs
508 are not available.

509 Moreover, this toolset is not specific to any planetary body nor specific landforms, thus is compatible with every
510 planet or moon imagery, if provided images are georeferenced and the corresponding reference system is passed to
511 the tool.

512 **Acknowledgments:** The authors declare no conflicts of interest.

513 **Funding:** This study is within the Europlanet 2024 RI and EXPLORE project, and it has received funding from the
514 European Union's Horizon 2020 research and innovation programme under grant agreement No 871149 and No
515 101004214.

516 **Data Availability Statement:**

517

518 **Open Research**

519 The original data used for this study are available at publicly data archive NASA PDS Geoscience Node Orbital
520 Data Explorer (ODE) (PDS Geosciences Nodes, 2021).

521 Datasets for this research are available in these in-text data citation references: (Nodjoumi, 2021b) with license
522 GPLv2+ and available at: <https://doi.org/10.5281/zenodo.5734912>

523 Software for this research is available in these in-text data citation references: (Nodjoumi, 2021c) with license
524 GPLv2+ and available at: <https://doi.org/10.5281/zenodo.5734621>

525 All base images of the figures have been prepared using QGIS software 3.16 LTS and then processed with Affinity
526 Publisher 1.1.

527

528 **References**

529 Acharya, G., De Smedt, F., & Long, N. T. (2006). Assessing landslide hazard in GIS: A case study from Rasuwa,
530 Nepal. *Bulletin of Engineering Geology and the Environment*, 65(1), 99–107.

531 <https://doi.org/10.1007/s10064-005-0025-y>

- 532 Alexandrov, O., & Beyer, R. A. (2018). Multiview Shape-From-Shading for Planetary Images. *Earth and Space*
533 *Science*, 5(10), 652–666. <https://doi.org/10.1029/2018EA000390>
- 534 Allemand, P., Delacourt, C., Gasperini, D., Kasperski, J., & Pothérat, P. (2011). Thirty Years of Evolution of the
535 Sedrun Landslide (Switzerland) from Multitemporal Orthorectified Aerial Images, Differential Digital
536 Terrain Models and Field Data. *International Journal of Remote Sensing Applications*, 5, 7.
- 537 Alonso, E. E., Pinyol, N. M., & Puzrin, A. M. (2010). Catastrophic Slide: Vaiont Landslide, Italy. In E. E. Alonso,
538 N. M. Pinyol, & A. M. Puzrin, *Geomechanics of Failures. Advanced Topics* (pp. 33–81). Springer
539 Netherlands. https://doi.org/10.1007/978-90-481-3538-7_2
- 540 Anderson Jeff & Deborah Lee Soltesz. (2003, June 11). *USGS Isis: Logical Cube Format Guide*.
541 <https://Isis.Astrogeology.Usgs.Gov/>.
542 <https://isis.astrogeology.usgs.gov/documents/LogicalCubeFormatGuide/LogicalCubeFormatGuide.html>
- 543 Aye, K.-M., Schwamb, M. E., Portyankina, G., Hansen, C. J., McMaster, A., Miller, G. R. M., Carstensen, B.,
544 Snyder, C., Parrish, M., Lynn, S., Mai, C., Miller, D., Simpson, R. J., & Smith, A. M. (2019). Planet Four:
545 Probing springtime winds on Mars by mapping the southern polar CO₂ jet deposits. *Icarus*, 319, 558–598.
546 <https://doi.org/10.1016/j.icarus.2018.08.018>
- 547 Bardabelias, N., Holt, J., & Christoffersen, M. (2020). Potential Detection of Martian Lava Tubes from Mars Global
548 Cave Candidate Catalog Skylight Locations Using SHARAD. *3rd International Planetary Caves*
549 *Conference*, 2197, 1068.
- 550 Barlow, N. G., Ferguson, S. N., Horstman, R. M., & Maine, A. (2017). Comparison of central pit craters on Mars,
551 Mercury, Ganymede, and the Saturnian satellites. *Meteoritics & Planetary Science*, 52(7), 1371–1387.
552 <https://doi.org/10.1111/maps.12857>
- 553 Barrett, A. M., Balme, M. R., Woods, M., Karachalios, S., Petrocelli, D., Joudrier, L., & Sefton-Nash, E. (2022).
554 NOAH-H, a deep-learning, terrain classification system for Mars: Results for the ExoMars Rover candidate
555 landing sites. *Icarus*, 371, 114701. <https://doi.org/10.1016/j.icarus.2021.114701>
- 556 Benedix, G. K., Lagain, A., Chai, K., Meka, S., Anderson, S., Norman, C., Bland, P. A., Paxman, J., Towner, M. C.,
557 & Tan, T. (2020). Deriving Surface Ages on Mars Using Automated Crater Counting. *Earth and Space*
558 *Science*, 7(3). <https://doi.org/10.1029/2019EA001005>

- 559 Blamont, J. (2014). A roadmap to cave dwelling on the Moon and Mars. *Advances in Space Research*, 54(10),
560 2140–2149. <https://doi.org/10.1016/j.asr.2014.08.019>
- 561 Bridge, J., & Demicco, R. (2008). *Earth Surface Processes, Landforms and Sediment Deposits*. 835.
- 562 Brierley, G., Fryirs, K., Reid, H., & Williams, R. (2021). The dark art of interpretation in geomorphology.
563 *Geomorphology*, 390, 107870. <https://doi.org/10.1016/j.geomorph.2021.107870>
- 564 Brust, C. A., Käding, C., & Denzler, J. (2019). Active learning for deep object detection. *VISIGRAPP 2019 -*
565 *Proceedings of the 14th International Joint Conference on Computer Vision, Imaging and Computer*
566 *Graphics Theory and Applications*, 5, 181–190. <https://doi.org/10.5220/0007248601810190>
- 567 Cahalan, M. D., & Milewski, A. M. (2018). Sinkhole formation mechanisms and geostatistical-based prediction
568 analysis in a mantled karst terrain. *CATENA*, 165, 333–344. <https://doi.org/10.1016/j.catena.2018.02.010>
- 569 Chappaz, L., Sood, R., Melosh, H. J., Howell, K. C., Blair, D. M., Milbury, C., & Zuber, M. T. (2017). Evidence of
570 large empty lava tubes on the Moon using GRAIL gravity: Evidence of Lunar Lava Tubes From GRAIL.
571 *Geophysical Research Letters*, 44(1), 105–112. <https://doi.org/10.1002/2016GL071588>
- 572 Chen, M., Lei, M., Liu, D., Zhou, Y., Zhao, H., & Qian, K. (2017). Morphological Features-Based Descriptive Index
573 System for Lunar Impact Craters. *ISPRS International Journal of Geo-Information*, 7(1), 5.
574 <https://doi.org/10.3390/ijgi7010005>
- 575 Cruikshank, D. P., & Wood, C. A. (1972). Lunar rilles and Hawaiian volcanic features: Possible analogues. *The*
576 *Moon*, 3(4), 412–447. <https://doi.org/10.1007/BF00562463>
- 577 Cushing, G. E. (2017). Mars Global Cave Candidate Catalog (MGC3)[abstract 3708]. *Astrobiology Science*
578 *Conference, Lunar and Planetary Institute, Houston. Available Online at [https://www. Hou. Usra.](https://www.hou.usra.edu/Meetings/Abscon2017/Pdf/3708.Pdf)*
579 *Edu/Meetings/Abscon2017/Pdf/3708. Pdf.*
- 580 Cushing, G. E., Okubo, C. H., & Titus, T. N. (2015). Atypical pit craters on Mars: New insights from THEMIS,
581 CTX, and HiRISE observations: ATYPICAL PIT CRATERS ON MARS. *Journal of Geophysical*
582 *Research: Planets*, 120(6), 1023–1043. <https://doi.org/10.1002/2014JE004735>
- 583 Cushing, G. E., & Titus, T. N. (2010). Caves on Mars: Candidate Sites for Astrobiological Exploration.
584 *Astrobiology Science Conference, 2010*, 2–3.
- 585 Cushing, G. E., Titus, T. N., Wynne, J. J., & Christensen, P. R. (2007). THEMIS observes possible cave skylights
586 on Mars. *Geophysical Research Letters*, 34(17), L17201. <https://doi.org/10.1029/2007GL030709>

- 587 De Blasio, F. V. (2011). Landslides in Valles Marineris (Mars): A possible role of basal lubrication by sub-surface
588 ice. *Planetary and Space Science*, 59(13), 1384–1392. <https://doi.org/10.1016/J.PSS.2011.04.015>
- 589 Díaz Michelena, M., Kilian, R., Baeza, O., Rios, F., Rivero, M. Á., Mesa, J. L., González, V., Ordoñez, A. A.,
590 Langlais, B., Rocca, M. C. L., & Acevedo, R. D. (2020). The formation of a giant collapse caprock
591 sinkhole on the Barda Negra plateau basalts (Argentina): Magnetic, mineralogical and morphostructural
592 evidences. *Geomorphology*, 367, 107297. <https://doi.org/10.1016/j.geomorph.2020.107297>
- 593 DiPietro, J. A. (2013). The Tortoise and the Hare. *Landscape Evolution in the United States*, 3–14.
594 <https://doi.org/10.1016/B978-0-12-397799-1.00001-4>
- 595 *Docker overview*. (2021, November 12). Docker Documentation. <https://docs.docker.com/get-started/overview/>
- 596 Duhart, P., Sepúlveda, V., Garrido, N., Mella, M., Quiroz, D., Fernández, J., Moreno, H., & Hermosilla, G. (2019).
597 *The Santa Lucía landslide disaster, Chaitén-Chile: Origin and effects*. 9.
- 598 Dundar, M., Ehlmann, B. L., & Leask, E. K. (2019). Machine-Learning-Driven New Geologic Discoveries at Mars
599 Rover Landing Sites: Jezero and NE Syrtis. *ArXiv:1909.02387 [Astro-Ph, Stat]*.
600 <http://arxiv.org/abs/1909.02387>
- 601 ESRI technical document. (1998). *ESRI Shapefile Technical Description*.
602 <https://www.esri.com/content/dam/esrisites/sitecore->
603 <archive/Files/Pdfs/library/whitepapers/pdfs/shapefile.pdf>.
604 <https://www.esri.com/content/dam/esrisites/sitecore->
605 <archive/Files/Pdfs/library/whitepapers/pdfs/shapefile.pdf>
- 606 Evans, I. S. (2012). Geomorphometry and landform mapping: What is a landform? *Geomorphology*, 137(1), 94–106.
607 <https://doi.org/10.1016/j.geomorph.2010.09.029>
- 608 Ferrill, D. A., Wyrick, D. Y., Morris, A. P., Sims, D. W., & Franklin, N. M. (2004). Dilational fault slip and pit
609 chain formation on Mars. *GSA Today*, 14(10), 4. <https://doi.org/10.1130/1052->
610 [5173\(2004\)014<4:DFSAPC>2.0.CO;2](5173(2004)014<4:DFSAPC>2.0.CO;2)
- 611 Ferrill, D. A., Wyrick, D. Y., & Smart, K. J. (2011). Coseismic, dilational-fault and extension-fracture related pit
612 chain formation in Iceland: Analog for pit chains on Mars. *Lithosphere*, 3(2), 133–142.
613 <https://doi.org/10.1130/L123.1>
- 614 Geomorphological mapping. (2013). *Geomorphological Techniques*, 10.

- 615 Ghorbanzadeh, O., Blaschke, T., Gholamnia, K., Meena, S., Tiede, D., & Aryal, J. (2019). Evaluation of Different
616 Machine Learning Methods and Deep-Learning Convolutional Neural Networks for Landslide Detection.
617 *Remote Sensing*, *11*(2), 196. <https://doi.org/10.3390/rs11020196>
- 618 Gillies, S. & others. (2021). *Rasterio: Geospatial raster I/O for Python programmers*. Mapbox.
619 <https://github.com/rasterio/rasterio>
- 620 Grace, R. K., Anitha, J., Sivaramakrishnan, R., & Sivakumari, M. S. S. (2021). *Crop and Weed Classification Using*
621 *Deep Learning*. 4.
- 622 Grant, J. A., Irwin, R. P., Grotzinger, J. P., Milliken, R. E., Tornabene, L. L., McEwen, A. S., Weitz, C. M.,
623 Squyres, S. W., Glotch, T. D., & Thomson, B. J. (2008). HiRISE imaging of impact megabreccia and sub-
624 meter aqueous strata in Holden Crater, Mars. *Geology*, *36*(3), 195. <https://doi.org/10.1130/G24340A.1>
- 625 Greeley, R. (1971). Lava tubes and channels in the lunar Marius Hills. *The Moon*, *3*(3), 289–314.
626 <https://doi.org/10.1007/BF00561842>
- 627 Guallini, L., Rossi, A. P., Forget, F., Marinangeli, L., Lauro, S. E., Pettinelli, E., Seu, R., & Thomas, N. (2018).
628 Regional stratigraphy of the south polar layered deposits (Promethei Lingula, Mars): “Discontinuity-
629 bounded” units in images and radargrams. *Icarus*, *308*, 76–107.
630 <https://doi.org/10.1016/j.icarus.2017.08.030>
- 631 Guimpier, A., Conway, S. J., Mangeney, A., Lucas, A., Mangold, N., Peruzzetto, M., Pajola, M., Lucchetti, A.,
632 Munaretto, G., Sæmundsson, T., Johnsson, A., Le Deit, L., Grindrod, P., Davis, J., Thomas, N., &
633 Cremonese, G. (2021). Dynamics of recent landslides (<20 My) on Mars: Insights from high-resolution
634 topography on Earth and Mars and numerical modelling. *Planetary and Space Science*, *206*(July), 105303.
635 <https://doi.org/10.1016/j.pss.2021.105303>
- 636 Gutiérrez, F., Guerrero, J., & Lucha, P. (2008). A genetic classification of sinkholes illustrated from evaporite
637 paleokarst exposures in Spain. *Environmental Geology*, *53*(5), 993–1006. [https://doi.org/10.1007/s00254-](https://doi.org/10.1007/s00254-007-0727-5)
638 [007-0727-5](https://doi.org/10.1007/s00254-007-0727-5)
- 639 Hare, T. M., Rossi, A. P., Frigeri, A., & Marmo, C. (2018). Interoperability in planetary research for geospatial data
640 analysis. *Planetary and Space Science*, *150*, 36–42. <https://doi.org/10.1016/j.pss.2017.04.004>
- 641 Hargitai, H., & Kereszturi, Á. (2015a). *Encyclopedia of planetary landforms*. Springer.

- 642 Hargitai, H., & Kereszturi, Á. (Eds.). (2015b). Impact Crater. In *Encyclopedia of Planetary Landforms* (pp. 972–
643 972). Springer New York. https://doi.org/10.1007/978-1-4614-3134-3_100204
- 644 Haruyama, J., Hioki, K., Shirao, M., Morota, T., Hiesinger, H., van der Bogert, C. H., Miyamoto, H., Iwasaki, A.,
645 Yokota, Y., Ohtake, M., Matsunaga, T., Hara, S., Nakanotani, S., & Pieters, C. M. (2009). Possible lunar
646 lava tube skylight observed by SELENE cameras. *Geophysical Research Letters*, 36(21), L21206.
647 <https://doi.org/10.1029/2009GL040635>
- 648 Hasani, R., Lechner, M., Amini, A., Rus, D., & Grosu, R. (2020). Liquid Time-constant Networks.
649 *ArXiv:2006.04439 [Cs, Stat]*. <http://arxiv.org/abs/2006.04439>
- 650 He, K., Gkioxari, G., Dollár, P., & Girshick, R. (2018). Mask R-CNN. *ArXiv:1703.06870 [Cs]*.
651 <http://arxiv.org/abs/1703.06870>
- 652 Hipperson, M., Waldmann, I., Grindrod, P., & Nikolaou, N. (2020). *Mapping Mineralogical Distributions on Mars*
653 *with Unsupervised Machine Learning* [Other]. oral. <https://doi.org/10.5194/epsc2020-773>
- 654 *HiRISE | About HiRISE Digital Terrain Models*. (2021). <https://www.uahirise.org/dtm/about.php>
- 655 Hoerer, T., & Kuenzer, C. (2020). Object detection and image segmentation with deep learning on Earth observation
656 data: A review-part I: Evolution and recent trends. *Remote Sensing*, 12(10).
657 <https://doi.org/10.3390/rs12101667>
- 658 Hong, I. S., Yi, Y., Yu, J., & Haruyama, J. (2015). 3D modeling of lacus mortis pit crater with presumed interior
659 tube structure. *Journal of Astronomy and Space Sciences*, 32(2), 113–120.
660 <https://doi.org/10.5140/JASS.2015.32.2.113>
- 661 Hooper, D. M., & Smart, K. J. (2013). Characterization of Landslides on Mars and Implications for Possible Failure
662 Mechanisms. *Lunar and Planetary Science Conference*, 1719, 1795.
- 663 Horvath, T., Hayne, P., & Paige, D. (2020). Thermal Environments and Illumination in Lunar Pits and Lava Tubes.
664 *Lunar and Planetary Science Conference*, 2326, 1729.
- 665 Hu, Y., Xiao, J., Liu, L., Zhang, L., & Wang, Y. (2021). Detection of Small Impact Craters via Semantic
666 Segmenting Lunar Point Clouds Using Deep Learning Network. *Remote Sensing*, 13(9), 1826.
667 <https://doi.org/10.3390/rs13091826>
- 668 Hung, O., Leroueil, S., & Picarelli, L. (2014). The Varnes classification of landslide types, an update. *Landslides*,
669 11(2), 167–194. <https://doi.org/10.1007/s10346-013-0436-y>

- 670 James, L. A., Harden, C. P., & Clague, J. J. (2013). 13.1 Geomorphology of Human Disturbances, Climate Change,
671 and Hazards. In *Treatise on Geomorphology* (pp. 1–13). Elsevier. [https://doi.org/10.1016/B978-0-12-](https://doi.org/10.1016/B978-0-12-374739-6.00339-0)
672 [374739-6.00339-0](https://doi.org/10.1016/B978-0-12-374739-6.00339-0)
- 673 Jiang, F. (2020). Criteria of sinkhole formation in soils from physical models. *Bulletin of Engineering Geology and*
674 *the Environment*, 79(7), 3833–3841. <https://doi.org/10.1007/s10064-020-01768-0>
- 675 Kaku, T., Haruyama, J., Miyake, W., Kumamoto, A., Ishiyama, K., Nishibori, T., Yamamoto, K., Crites, S. T.,
676 Michikami, T., Yokota, Y., Sood, R., Melosh, H. J., Chappaz, L., & Howell, K. C. (2017). Detection of
677 Intact Lava Tubes at Marius Hills on the Moon by SELENE (Kaguya) Lunar Radar Sounder: Intact Lunar
678 Lava Tube Detection by LRS. *Geophysical Research Letters*, 44(20), 10,155-10,161.
679 <https://doi.org/10.1002/2017GL074998>
- 680 Kalogirou, S. A. (2009). Chapter two—Environmental Characteristics. In S. A. Kalogirou (Ed.), *Solar Energy*
681 *Engineering* (pp. 49–762). Academic Press. <https://doi.org/10.1016/B978-0-12-374501-9.00002-9>
- 682 Kumar, P., Rawat, J. S., Rehman, S., Sajjad, H., Rani, M., Mohanto, K. K., Rai, O., & Tripathy, B. (2019).
683 *Exploring Geomorphic Processes and Martian Gale Crater Topography on Mars using CTX and HiRISE*
684 *Express Image Dataset* [Preprint]. Geosciences – Applied Geology. <https://doi.org/10.5194/essd-2019-4>
- 685 Lacerda, W., Ehrlich, M., Fontoura, S., & Sayão, A. (2004). *Landslides: Evaluation and Stabilization/Glisement de*
686 *Terrain: Evaluation et Stabilisation, Set of 2 Volumes: Proceedings of the Ninth International Symposium*
687 *on Landslides, June 28 -July 2, 2004 Rio de Janeiro, Brazil*. CRC Press. <https://doi.org/10.1201/b16816>
- 688 Laura, J., Acosta, A., Addair, T., Adoram-Kershner, L., Alexander, J., Alexandrov, O., Alley, S., Anderson, D.,
689 Anderson, J., Anderson, J., Annex, A., Archinal, B., Austin, C., Backer, J., Barrett, J., Bauers, J., Becker,
690 K., Becker, T., Bennett, G., ... Young, A. (2021). *Integrated Software for Imagers and Spectrometers*.
691 Zenodo. <https://doi.org/10.5281/zenodo.5347823>
- 692 Le Mouélic, S., Enguehard, P., Schmitt, H. H., Caravaca, G., Seignovert, B., Mangold, N., Combe, J.-P., & Civet, F.
693 (2020). Investigating Lunar Boulders at the Apollo 17 Landing Site Using Photogrammetry and Virtual
694 Reality. *Remote Sensing*, 12(11), 1900. <https://doi.org/10.3390/rs12111900>
- 695 Lee, C. (2019). Automated crater detection on Mars using deep learning. *Planetary and Space Science*, 170, 16–28.
696 <https://doi.org/10.1016/j.pss.2019.03.008>

- 697 L veill , R. J., & Datta, S. (2010). Lava tubes and basaltic caves as astrobiological targets on Earth and Mars: A
698 review. *Planetary and Space Science*, 58(4), 592–598. <https://doi.org/10.1016/j.pss.2009.06.004>
- 699 Lin, C.-W., Shieh, C.-L., Yuan, B.-D., Shieh, Y.-C., Liu, S.-H., & Lee, S.-Y. (2004). Impact of Chi-Chi earthquake
700 on the occurrence of landslides and debris flows: Example from the Chenyulan River watershed, Nantou,
701 Taiwan. *Engineering Geology*, 71(1–2), 49–61. [https://doi.org/10.1016/S0013-7952\(03\)00125-X](https://doi.org/10.1016/S0013-7952(03)00125-X)
- 702 Liu, J. G., Mason, P. J., Clerici, N., Chen, S., Davis, A., Miao, F., Deng, H., & Liang, L. (2004). Landslide hazard
703 assessment in the Three Gorges area of the Yangtze river using ASTER imagery: Zigui–Badong.
704 *Geomorphology*, 61(1–2), 171–187. <https://doi.org/10.1016/j.geomorph.2003.12.004>
- 705 Lohse, V., Heipke, C., & Kirk, R. L. (2006). Derivation of planetary topography using multi-image shape-from-
706 shading. *Planetary and Space Science*, 54(7), 661–674. <https://doi.org/10.1016/j.pss.2006.03.002>
- 707 Luebke, D. (2008). CUDA: Scalable parallel programming for high-performance scientific computing. *2008 5th*
708 *IEEE International Symposium on Biomedical Imaging: From Nano to Macro*, 836–838.
709 <https://doi.org/10.1109/ISBI.2008.4541126>
- 710 Luzzi, E., Rossi, A. P., Carli, C., & Altieri, F. (2020). Tectono-Magmatic, Sedimentary, and Hydrothermal History
711 of Arsinoes and Pyrrhae Chaos, Mars. *Journal of Geophysical Research: Planets*, 125(12).
712 <https://doi.org/10.1029/2019JE006341>
- 713 Martinot, M., Besse, S., Flahaut, J., Quantin-Nataf, C., Lozac’h, L., & van Westrenen, W. (2018). Mineralogical
714 diversity and geology of Humboldt crater derived using Moon Mineralogy Mapper data. *Journal of*
715 *Geophysical Research: Planets*, 123(2), 612–629.
- 716 Massa, F., & Girshick, R. (2018). *maskrcnn-benchmark: Fast, modular reference implementation of Instance*
717 *Segmentation and Object Detection algorithms in PyTorch*. [https://github.com/facebookresearch/maskrcnn-](https://github.com/facebookresearch/maskrcnn-benchmark/)
718 [benchmark/](https://github.com/facebookresearch/maskrcnn-benchmark/)
- 719 McEwen, A. S., Eliason, E. M., Bergstrom, J. W., Bridges, N. T., Hansen, C. J., Delamere, W. A., Grant, J. A.,
720 Gulick, V. C., Herkenhoff, K. E., Keszthelyi, L., Kirk, R. L., Mellon, M. T., Squyres, S. W., Thomas, N., &
721 Weitz, C. M. (2007). Mars Reconnaissance Orbiter’s High Resolution Imaging Science Experiment
722 (HiRISE). *Journal of Geophysical Research*, 112(E5), E05S02. <https://doi.org/10.1029/2005JE002605>

- 723 McEwen, A. S., Schaefer, E. I., Dundas, C. M., Sutton, S. S., Tamppari, L. K., & Chojnacki, M. (2021). Mars:
724 Abundant Recurring Slope Lineae (RSL) Following the Planet-Encircling Dust Event (PEDE) of 2018.
725 *Journal of Geophysical Research: Planets*, 126(4). <https://doi.org/10.1029/2020JE006575>
- 726 Merghadi, A., Yunus, A. P., Dou, J., Whiteley, J., ThaiPham, B., Bui, D. T., Avtar, R., & Abderrahmane, B. (2020).
727 Machine learning methods for landslide susceptibility studies: A comparative overview of algorithm
728 performance. *Earth-Science Reviews*, 207, 103225. <https://doi.org/10.1016/j.earscirev.2020.103225>
- 729 Merkel, D. (2014). Docker: Lightweight linux containers for consistent development and deployment. *Linux*
730 *Journal*, 2014(239), 2.
- 731 Micheletti, N., Chandler, J. H., & Lane, S. N. (2015). Structure from Motion (SfM) Photogrammetry.
732 *Geomorphological Techniques*, 12.
- 733 Michikami, T., Hagermann, A., Miyamoto, H., Miura, S., Haruyama, J., & Lykawka, P. S. (2014). Impact cratering
734 experiments in brittle targets with variable thickness: Implications for deep pit craters on Mars. *Planetary*
735 *and Space Science*, 96, 71–80. <https://doi.org/10.1016/j.pss.2014.03.010>
- 736 Milkovich, S. M., Plaut, J. J., Safaeinili, A., Picardi, G., Seu, R., & Phillips, R. J. (2009). Stratigraphy of Promethei
737 Lingula, south polar layered deposits, Mars, in radar and imaging data sets. *Journal of Geophysical*
738 *Research*, 114(E3), E03002. <https://doi.org/10.1029/2008JE003162>
- 739 Miyamoto, H., Uehara, K., Murakawa, M., Sakanashi, H., Nosato, H., Kouyama, T., & Nakamura, R. (2018). Object
740 detection in satellite imagery using 2-step convolutional neural networks. *International Geoscience and*
741 *Remote Sensing Symposium (IGARSS), 2018-July*, 1268–1271.
742 <https://doi.org/10.1109/IGARSS.2018.8518587>
- 743 Mougini-Mark, P. J. (2004). Geometry of Martian impact craters: First results from an interactive software
744 package. *Journal of Geophysical Research*, 109(E8), E08006. <https://doi.org/10.1029/2003JE002147>
- 745 Muller, J.-P., Tao, Y., Putri, A. R. D., & Conway, S. J. (2021). 3D MULTI-RESOLUTION MAPPING OF MARS
746 USING CASP-GO ON HRSC, CRISM, CTX AND HIRISE. *The International Archives of the*
747 *Photogrammetry, Remote Sensing and Spatial Information Sciences*, XLIII-B3-2021, 667–671.
748 <https://doi.org/10.5194/isprs-archives-XLIII-B3-2021-667-2021>
- 749 Nagle-McNaughton, T., McClanahan, T., & Scuderi, L. (2020). PlaNet: A Neural Network for Detecting Transverse
750 Aeolian Ridges on Mars. *Remote Sensing*, 12(21), 3607. <https://doi.org/10.3390/rs12213607>

- 751 Napieralski, J., Barr, I., Kamp, U., & Kervyn, M. (2013). 3.8 Remote Sensing and GIScience in Geomorphological
752 Mapping. In *Treatise on Geomorphology* (pp. 187–227). Elsevier. [https://doi.org/10.1016/B978-0-12-](https://doi.org/10.1016/B978-0-12-374739-6.00050-6)
753 [374739-6.00050-6](https://doi.org/10.1016/B978-0-12-374739-6.00050-6)
- 754 NASA. (2021). *NASA BRAILLE – Biologic and Resource Analog Investigations in Low Light Environments*.
755 <https://nasa-braille.org/>
- 756 Naß, A., Di, K., Elgner, S., van Gasselt, S., Hare, T., Hargitai, H., Karachevtseva, I., Kersten, E., Manaud, N.,
757 Roatsch, T., Rossi, A. P., Skinner Jr., J., & Wählich, M. (2017). PLANETARY CARTOGRAPHY AND
758 MAPPING: WHERE WE ARE TODAY, AND WHERE WE ARE HEADING FOR? *The International*
759 *Archives of the Photogrammetry, Remote Sensing and Spatial Information Sciences, XLII-3/W1*, 105–112.
760 <https://doi.org/10.5194/isprs-archives-XLII-3-W1-105-2017>
- 761 Naß, A., Massironi, M., Rossi, A., Penasa, L., Pozzobon, R., Brandt, C., Nodjoumi, G., Pondrelli, M., Galluzzi, V.,
762 Altieri, F., Frigeri, A., Carli, C., Giacomoni, L., Mege, D., Gurgurewicz, J., Tesson, P.-A., Marinangeli, L.,
763 van der Bogert, C. H., & Poehler, C. (2021). *Streamlining European Mapping Efforts: The Geologic*
764 *Mapping of Planetary Bodies (GMAP)*. 2610, 7034. <https://elib.dlr.de/142475/>
- 765 Naß, A., & van Gasselt, S. (2021). The geologic map of the Cassini quadrangle on the Moon: Planetary cartography
766 between science, efficacy and cartographic aesthetics. *International Journal of Cartography*, 7(2), 178–
767 183.
- 768 Nass, A., van Gasselt, S., Hare, T., & Hargitai, H. (2021). 50 Years of Sensor-Based Planetary Cartography: Review
769 and Perspectives. *Proceedings of the ICA*, 4, 1–8. <https://doi.org/10.5194/ica-proc-4-76-2021>
- 770 Nodjoumi, G. (2021a, October 13). *ImageProcessingUtils: Docker container, Jupyter Notebook and CLI*.
771 <https://doi.org/10.5281/zenodo.5566774>
- 772 Nodjoumi, G. (2021b). *DeepLandforms: A Deep Learning Computer Vision toolset applied to a prime use case for*
773 *mapping planetary skylights - ANc* [Data set]. <https://doi.org/10.5281/zenodo.5734912>
- 774 Nodjoumi, G. (2021c, November 29). *DeepLandforms: First Release*. <https://doi.org/10.5281/zenodo.5734621>
- 775 Nodjoumi, G., Pozzobon, R., & Rossi, A. P. (2021). DEEP LEARNING OBJECT DETECTION FOR MAPPING
776 CAVE CANDIDATES ON MARS: BUILDING UP THE MARS GLOBAL CAVE CANDIDATE
777 CATALOG (MGC³). *Lunar and Planetary Science Conference*, 2548.
778 <https://www.hou.usra.edu/meetings/lpsc2021/pdf/1316.pdf>

- 779 Open Geospatial Consortium. (2021). *OGC® GeoPackage Encoding Standard*. <https://www.geopackage.org/spec/>
- 780 Palafox, L. F., Hamilton, C. W., Scheidt, S. P., & Alvarez, A. M. (2017). Automated detection of geological
781 landforms on Mars using Convolutional Neural Networks. *Computers & Geosciences*, *101*, 48–56.
782 <https://doi.org/10.1016/j.cageo.2016.12.015>
- 783 Parente, M., Itoh, Y., & Saranathan, A. (2019). New CRISM Data Products for Improved Characterization and
784 Analysis of the Mars2020 Landing Site. *IGARSS 2019 - 2019 IEEE International Geoscience and Remote
785 Sensing Symposium*, 4911–4914. <https://doi.org/10.1109/IGARSS.2019.8899313>
- 786 Parise, M. (2019). Sinkholes. In *Encyclopedia of Caves* (pp. 934–942). Elsevier. [https://doi.org/10.1016/B978-0-12-
787 814124-3.00110-2](https://doi.org/10.1016/B978-0-12-814124-3.00110-2)
- 788 Paul, S., & Ganju, S. (2021). Flood Segmentation on Sentinel-1 SAR Imagery with Semi-Supervised Learning.
789 *ArXiv:2107.08369 [Cs]*. <http://arxiv.org/abs/2107.08369>
- 790 PDS Geosciences Nodes. (2021). *Orbital Data Explorer—Mars Holdings*.
791 https://ode.rsl.wustl.edu/odeholdings/Mars_holdings.html
- 792 Pham, M.-T., Courtrai, L., Friguet, C., Lefèvre, S., & Baussard, A. (2020). YOLO-Fine: One-Stage Detector of
793 Small Objects Under Various Backgrounds in Remote Sensing Images. *Remote Sensing*, *12*(15), 2501.
794 <https://doi.org/10.3390/rs12152501>
- 795 Pipan, T., & Culver, D. C. (2019). Chapter 107—Shallow subterranean habitats. In W. B. White, D. C. Culver, & T.
796 Pipan (Eds.), *Encyclopedia of Caves (Third Edition)* (pp. 896–908). Academic Press.
797 <https://doi.org/10.1016/B978-0-12-814124-3.00107-2>
- 798 Pondrelli, M., Frigeri, A., Marinangeli, L., Di Pietro, I., Pantaloni, M., Pozzobon, R., Nass, A., & Rossi, A. P.
799 (2020). *Geological and geomorphological mapping of Martian sedimentary deposits: An attempt to identify
800 current practices in mapping and representation* [Other]. oral. <https://doi.org/10.5194/epsc2020-232>
- 801 Rashno, A., Nazari, B., Sadri, S., & Saraee, M. (2017). Effective pixel classification of Mars images based on ant
802 colony optimization feature selection and extreme learning machine. *Neurocomputing*, *226*, 66–79.
803 <https://doi.org/10.1016/j.neucom.2016.11.030>
- 804 Redmon, J., Divvala, S., Girshick, R., & Farhadi, A. (2016). You only look once: Unified, real-time object detection.
805 *Proceedings of the IEEE Computer Society Conference on Computer Vision and Pattern Recognition*.
806 <https://doi.org/10.1109/CVPR.2016.91>

- 807 Robbins, S. J., & Hynek, B. M. (2014). The secondary crater population of Mars. *Earth and Planetary Science*
808 *Letters*, *400*(2012), 66–76. <https://doi.org/10.1016/j.epsl.2014.05.005>
- 809 Robinson, M. S., Brylow, S. M., Tschimmel, M., Humm, D., Lawrence, S. J., Thomas, P. C., Denevi, B. W.,
810 Bowman-Cisneros, E., Zerr, J., Ravine, M. A., Caplinger, M. A., Ghaemi, F. T., Schaffner, J. A., Malin, M.
811 C., Mahanti, P., Bartels, A., Anderson, J., Tran, T. N., Eliason, E. M., ... Hiesinger, H. (2010). Lunar
812 Reconnaissance Orbiter Camera (LROC) Instrument Overview. *Space Science Reviews*, *150*(1–4), 81–124.
813 <https://doi.org/10.1007/s11214-010-9634-2>
- 814 Robinson, M. S., Wagner, R. V., Speyerer, E. J., & Robinson, M. S. (2017). Exploring the Moon with Automated
815 Feature Detection. *Space Sci. Rev*, *129*(2), 2769.
- 816 Rousset, G., Despinoy, M., Schindler, K., & Mangeas, M. (2021). Assessment of Deep Learning Techniques for
817 Land Use Land Cover Classification in Southern New Caledonia. *Remote Sensing*, *13*(12), 2257.
818 <https://doi.org/10.3390/rs13122257>
- 819 Salese, F., Pondrelli, M., Neeseman, A., Schmidt, G., & Ori, G. G. (2019). Geological Evidence of Planet-Wide
820 Groundwater System on Mars. *Journal of Geophysical Research: Planets*, *124*(2), 374–395.
821 <https://doi.org/10.1029/2018JE005802>
- 822 Sargeant, H. M., Bickel, V. T., Honniball, C. I., Martinez, S. N., Rogaski, A., Bell, S. K., Czaplinski, E. C., Farrant,
823 B. E., Harrington, E. M., Tolometti, G. D., & Kring, D. A. (2020). Using Boulder Tracks as a Tool to
824 Understand the Bearing Capacity of Permanently Shadowed Regions of the Moon. *Journal of Geophysical*
825 *Research: Planets*, *125*(2). <https://doi.org/10.1029/2019JE006157>
- 826 Sauro, F., Pozzobon, R., Massironi, M., De Berardinis, P., Santagata, T., & De Waele, J. (2020). Lava tubes on
827 Earth, Moon and Mars: A review on their size and morphology revealed by comparative planetology.
828 *Earth-Science Reviews*, *209*, 103288. <https://doi.org/10.1016/j.earscirev.2020.103288>
- 829 Sauro, U. (2016). Dolines and Sinkholes: Aspects of Evolution and Problems of Classification. *Acta Carsologica*,
830 *32*(2). <https://doi.org/10.3986/ac.v32i2.335>
- 831 Servis, K., Lagain, A., Benedix, G., Flannery, D., Norman, C., Towner, M., & Paxman, J. (2020). *Automatic crater*
832 *detection over the Jezero crater area from HiRISE imagery* [Other]. *pico*.
833 <https://doi.org/10.5194/egusphere-egu2020-6269>

- 834 Sharma, R., & Srivastava, N. (2021). *Detection and classification of skylights on the flank of Elysium Mons, Mars*
835 [Preprint]. *Geology*. <https://doi.org/10.1002/essoar.10506123.1>
- 836 Silburt, A. (2019). *DeepMoon—Lunar Crater Counting Through Deep Learning* [Python].
837 <https://github.com/silburt/DeepMoon> (Original work published 2017)
- 838 Silburt, A., Ali-Dib, M., Zhu, C., Jackson, A., Valencia, D., Kissin, Y., Tamayo, D., & Menou, K. (2019). Lunar
839 Crater Identification via Deep Learning. *Icarus*, *317*, 27–38. <https://doi.org/10.1016/j.icarus.2018.06.022>
- 840 Sivakumar, V., Neelakantan, R., & Santosh, M. (2017). Lunar surface mineralogy using hyperspectral data:
841 Implications for primordial crust in the Earth–Moon system. *Geoscience Frontiers*, *8*(3), 457–465.
842 <https://doi.org/10.1016/j.gsf.2016.03.005>
- 843 Slaymaker, O., Spencer, T., & Embleton-Hamann, C. (2021). Recasting geomorphology as a landscape science.
844 *Geomorphology*, *384*, 107723. <https://doi.org/10.1016/j.geomorph.2021.107723>
- 845 Smith, Z., Tullis, J., Steele, K., & Malfavon, L. (2006). Martian Sinkholes: Implications for Large Scale Evaporite
846 Deposits. *37th Annual Lunar and Planetary Science Conference*, 1071.
- 847 Stepinski, T. F., Soumya Ghosh, & Vilalta, R. (2007). *Machine Learning for Automatic Mapping of Planetary*
848 *Surfaces*. <https://doi.org/10.13140/2.1.1518.9445>
- 849 Su, S., Fanara, L., Zhang, X., Gwinner, K., Hauber, E., & Oberst, J. (2021). DETECTING THE SOURCES OF ICE
850 BLOCK FALLS AT THE MARTIAN NORTH POLAR SCARPS BY ANALYSIS OF MULTI-
851 TEMPORAL HIRISE IMAGERY. *The International Archives of the Photogrammetry, Remote Sensing and*
852 *Spatial Information Sciences, XLIII-B3-2021*, 673–678. [https://doi.org/10.5194/isprs-archives-XLIII-B3-](https://doi.org/10.5194/isprs-archives-XLIII-B3-2021-673-2021)
853 [2021-673-2021](https://doi.org/10.5194/isprs-archives-XLIII-B3-2021-673-2021)
- 854 Sun, V. Z., & Stack, K. M. (2020). Geologic map of Jezero crater and the Nili Planum region, Mars. In *Geologic*
855 *map of Jezero crater and the Nili Planum region, Mars* (USGS Numbered Series No. 3464; Scientific
856 Investigations Map, Vol. 3464). U.S. Geological Survey. <https://doi.org/10.3133/sim3464>
- 857 Szegedy, C., Toshev, A., & Erhan, D. (2013). Deep Neural Networks for Object Detection. *Advances in Neural*
858 *Information Processing Systems 26 (NIPS 2013)*. <https://doi.org/10.1109/CVPR.2014.276>
- 859 Talukdar, S., Singha, P., Mahato, S., Pal, S., Liou, Y.-A., Rahman, A., & others. (2020). Land-use land-cover
860 classification by machine learning classifiers for satellite observations—A review. *Remote Sensing*, *12*(7),
861 1135.

- 862 Tempfli, K., Huurneman, G. C., Bakker, W. H., Janssen, L. L. F., Feringa, W. F., Gieske, A. S. M., Grabmaier, K.
863 A., Hecker, C. A., & Horn, J. A. van der. (2009). *Principles of remote sensing: An introductory textbook*.
864 ITC.
- 865 Tien Bui, D., Tuan, T. A., Klempe, H., Pradhan, B., & Revhaug, I. (2016). Spatial prediction models for shallow
866 landslide hazards: A comparative assessment of the efficacy of support vector machines, artificial neural
867 networks, kernel logistic regression, and logistic model tree. *Landslides*. [https://doi.org/10.1007/s10346-](https://doi.org/10.1007/s10346-015-0557-6)
868 [015-0557-6](https://doi.org/10.1007/s10346-015-0557-6)
- 869 Tirsch, D., Voigt, J. R. C., Viviano, C. E., Bishop, J. L., Lane, M. D., Tornabene, L. L., & Loizeau, D. (2021).
870 Spatial Trends in Mineral Abundances across Tyrrhena Terra on Mars derived from Geomorphological and
871 Mineralogical Mapping. *EGU General Assembly Conference Abstracts*, EGU21-7440.
- 872 Tsibulskaya, V., Hepburn, A. J., Hubbard, B., & Holt, T. (2020). Surficial geology and geomorphology of Greg
873 crater, Promethei Terra, Mars. *Journal of Maps*, *16*(2), 524–533.
874 <https://doi.org/10.1080/17445647.2020.1785343>
- 875 *Ultralytics/yolov5*. (2021). [Python]. Ultralytics. <https://github.com/ultralytics/yolov5> (Original work published
876 2020)
- 877 Van Den Eeckhaut, M., Poesen, J., Govers, G., Verstraeten, G., & Demoulin, A. (2007). Characteristics of the size
878 distribution of recent and historical landslides in a populated hilly region. *Earth and Planetary Science*
879 *Letters*, *256*(3–4), 588–603. <https://doi.org/10.1016/j.epsl.2007.01.040>
- 880 van der Bogert, C. H., & Ashley, J. W. (2015). Skylight. In H. Hargitai & Á. Kereszturi, *Encyclopedia of Planetary*
881 *Landforms* (pp. 1–7). Springer New York. https://doi.org/10.1007/978-1-4614-9213-9_342-2
- 882 Wada, K. (2021). *Labelme: Image Polygonal Annotation with Python*. <https://doi.org/10.5281/zenodo.5711226>
- 883 Wang, S., Fan, Z., Li, Z., Zhang, H., & Wei, C. (2020). An Effective Lunar Crater Recognition Algorithm Based on
884 Convolutional Neural Network. *Remote Sensing*, *12*(17), 2694. <https://doi.org/10.3390/rs12172694>
- 885 Wang, Y., Wu, B., Xue, H., Li, X., & Ma, J. (2021). An Improved Global Catalog of Lunar Impact Craters (≥ 1 km)
886 with 3D Morphometric Information and Updates on Global Crater Analysis. *Journal of Geophysical*
887 *Research: Planets*, *126*(9), e2020JE006728.
- 888 Watkins, R., Jolliff, B., Lawrence, S., Hayne, P., & Ghent, R. (2017). *Boulder distributions at legacy landing sites:*
889 *Assessing regolith production rates and landing site hazards*.

- 890 Watters, W. A., Geiger, L. M., Fendrock, M., & Gibson, R. (2015). Morphometry of small recent impact craters on
891 Mars: Size and terrain dependence, short-term modification. *Journal of Geophysical Research: Planets*,
892 *120*(2), 226–254.
- 893 Whitten, J. L., & Martin, E. S. (2019). Icelandic Pit Chains as Planetary Analogs: Using Morphologic Measurements
894 of Pit Chains to Determine Regolith Thickness. *Journal of Geophysical Research: Planets*, *124*(11), 2983–
895 2999. <https://doi.org/10.1029/2019JE006099>
- 896 Wilhelm, T., Geis, M., Püttschneider, J., Sievernich, T., Weber, T., Wohlfarth, K., & Wöhler, C. (2020).
897 DoMars16k: A Diverse Dataset for Weakly Supervised Geomorphologic Analysis on Mars. *Remote*
898 *Sensing*, *12*(23), 3981. <https://doi.org/10.3390/rs12233981>
- 899 Wu, B., Li, F., Hu, H., Zhao, Y., Wang, Y., Xiao, P., Li, Y., Liu, W. C., Chen, L., Ge, X., & others. (2020).
900 Topographic and Geomorphological Mapping and Analysis of the Chang'E-4 Landing Site on the Far Side
901 of the Moon. *Photogrammetric Engineering & Remote Sensing*, *86*(4), 247–258.
- 902 Wu, Y., Kirillov, A., Massa, F., Lo, W.-Y., & Girshick, R. (2019a). *Detectron2 is FAIR's next-generation platform*
903 *for object detection, segmentation and other visual recognition tasks.*
904 <https://github.com/facebookresearch/detectron2>
- 905 Wu, Y., Kirillov, A., Massa, F., Lo, W.-Y., & Girshick, R. (2019b). *Detectron2/MODEL_ZOO.md at main ·*
906 *facebookresearch/detectron2.*
907 https://github.com/facebookresearch/detectron2/blob/main/MODEL_ZOO.md
- 908 Wu, Y., Kirillov, A., Massa, F., Lo, W.-Y., Girshick, R., & Facebook, Inc. (2020). *facebookresearch/detectron2:*
909 *Detectron2 is FAIR's next-generation platform for object detection and segmentation.*
910 <https://github.com/facebookresearch/detectron2>
- 911 Wyrick, D. (2004). Distribution, morphology, and origins of Martian pit crater chains. *Journal of Geophysical*
912 *Research*, *109*(E6), E06005. <https://doi.org/10.1029/2004JE002240>
- 913 Xiao, Z., Zeng, Z., & Komatsu, G. (2014). A global inventory of central pit craters on the Moon: Distribution,
914 morphology, and geometry. *Icarus*, *227*, 195–201. <https://doi.org/10.1016/j.icarus.2013.09.019>
- 915 Yousefi, S., Pourghasemi, H. R., Emami, S. N., Pouyan, S., Eskandari, S., & Tiefenbacher, J. P. (2020). A machine
916 learning framework for multi-hazards modeling and mapping in a mountainous area. *Scientific Reports*,
917 *10*(1), 12144. <https://doi.org/10.1038/s41598-020-69233-2>

- 918 Youssef, A. M., El-Kaliouby, H., & Zabramawi, Y. A. (2012). Sinkhole detection using electrical resistivity
919 tomography in Saudi Arabia. *Journal of Geophysics and Engineering*, 9(6), 655–663.
920 <https://doi.org/10.1088/1742-2132/9/6/655>
- 921 Zhang, A., Lipton, Z. C., Li, M., & Smola, A. J. (2021). 4.4.3 Underfitting or Overfitting? In *Dive into Deep*
922 *Learning* (pp. 146–147). <http://arxiv.org/abs/2106.11342>
- 923 Zhao, Z. Q., Zheng, P., Xu, S. T., & Wu, X. (2019). Object Detection with Deep Learning: A Review. In *IEEE*
924 *Transactions on Neural Networks and Learning Systems* (Vol. 30, Issue 11, pp. 3212–3232).
925 <https://doi.org/10.1109/TNNLS.2018.2876865>
- 926
- 927

Earth and Space Science

Supporting Information for

DeepLandforms: A Deep Learning Computer Vision toolset applied to a prime use case for mapping planetary skylights

Giacomo Nodjoumi^{1*}, Riccardo Pozzobon^{2,3}, Francesco Sauro⁴, Angelo Pio Rossi¹

¹Jacobs University Bremen gGmbH, Bremen, Germany

²INAF-Astronomical Observatory of Padova, Padova, Italy

³Department of Geosciences, University of Padova, Padova, Italy

⁴Department of Biological, Geological and Environmental Sciences, University of Bologna, Bologna, Italy

Contents of this file

Text S1 to S7

Figures S1 to S11

Tables S1 to S5

Introduction

The following supporting information includes general insights on Deep Learning Object Detection and Instance Segmentation methodologies and their state-of-the-art (Text S1) including a brief overview of Facebook's Detectron2 (Text S2). In Text S3 is described the dataset preparation workflow while in Text S4 are described Image Masks with an example in Figure S1.

In Text S5 are listed the components of the *DeepLandforms* toolset that can be found in the repository with a more detailed description of the jupyter notebooks available in Text S6.

The Text S7 contains the Mask_rcnn_R_50_FPN model configuration used in this work.

Figures S2 and S3 contains additional examples of the comparison between brightness and DTM profiles for pits.

In Figure S4 are showed examples of multiple detections of the same landforms related to source images with different acquisition angle.

Figures from S5 to S8 show several examples of the results obtained by using the manual approach of Cushing et al., compared to the results obtained by using the tools based on the object detection (DeepLandforms-YOLOv5) and Instance Segmentation (DeepLandforms) methodologies.

Figure S9 to S11 shows an example of a training session monitored through tensorboard, in which are visible all the mAP for object detection and instance segmentation for each class type.

A summary of the main parameters essential to landforms description are available in Table S1.

Table S2 contains a list of acronyms found in the main document and here.

In Table S3 are resumed the ranges of the model training parameters while in Table S4 are summarized the average results obtained at the end of the model training, same as Figures S9 to S11.

The list of all the names of the source images used in this work and downloaded from the PDS Geosciences Node Orbital Data Explorer (ODE).

Text S1. State of the art in Deep Learning Object Detection and Segmentation methodologies

An Artificial Neural Network (ANN) can be intended as a complex computational model, inspired by biological neural networks, composed of "digital neurons" and used to easily solve complex problems. For Deep Learning (DL) we mean a Machine Learning (ML) technique that makes use of an artificial neural network based on a layered structure with different degrees of interconnection in which the first level is the data entry, the last is the level of results return and the intermediate levels can be defined as decision-making levels or a set of logical choices implemented autonomously by the artificial network (Hoeser & Kuenzer, 2020).

A Convolutional Neural Network (CNN) (Dhillon & Verma, 2020; Gu et al., 2018) is an algorithm that take in an input image, assigns importance (*weights*) to aspects/objects and learn how to differentiate among other aspects/objects and is composed mainly by Convolution Layers, Pooling Layers and Fully Connected Layers in different configurations.

There are several well-known and widely used CNN (Hoeser & Kuenzer, 2020), most used are R-CNN-based for object detection (Fast-R-CNN, Faster-R-CNN) (Girshick, 2015; Ren et al., 2016) and Instance Segmentation(Mask-R-CNN) (Chen et al., 2019; He et al., 2018, p.; Massa & Girshick, 2018), YOLO (Pham et al., 2020), ResNet (Targ et al., 2016), MobileSSD (Howard et al., 2017). and are particularly used in Computer Vision (CV) with applications for the classification and recognition of objects present. in an image or video, both static and dynamic, for example the recognition of license plates, faces, object tracking, etc.

When training new models, it is possible to train them from scratch only if a custom training dataset is big enough, otherwise an underfitting problem will occur.

A model is considered overfitted when it has excellent performance on trained data but poor performance on newer data while is considered underfitted when it has global poor performances related to a very small dataset (Amazon Machine Learning, 2021; Zhang et al., 2021).

Almost all state-of-the-art public Earth-related datasets such as MS COCO, ImageNet (Deng et al., 2009; Lin et al., 2015), contain up to several millions of labels and associated images and are commonly used for training above-mentioned architectures, granting a very good generalization of the problem of detection and segmentation without underfitting or overfitting. Models trained with such datasets are used to compute benchmarks for those architectures and evaluate their performance. Those benchmarks are further used as reference for newer and modified architectures (Wu et al., 2019b).

A possible solution to overfitting and underfitting is a method named Transfer Learning (Neyshabur et al., 2020, 2021; Tan et al., 2018; Weiss et al., 2016) in which a model pre-trained on a very large dataset, such as the above-mentioned ones, is partially re-trained to adapt it to a custom dataset. For instance, an object detection model pre-trained on a large dataset containing thousands of trees images, can be re-trained on a custom smaller dataset containing plants.

An oversimplification of the training phase of a model consists of several cycles (*epochs*) in which data (*batch size*) are fed to the network, weights are computed at each layer, an output is produced, and an estimation of the error (*loss*) is computed. Then the difference between the obtained result and the correct one is backpropagated to each layer in order to adjust the corresponding weights. This process is regulated by a parameter called *learning rate*, a value between 0 and 1 that is multiplied by the loss gradient rate e computed difference in order to avoid over adaptation to that specific data, losing effectiveness to other data (Google Developers, 2021)

The common evaluation metric used in object detection and image segmentation based on COCO format is the mean Average Precision (mAP). This parameter can be described as the area under the precision-recall curve. Precision is the parameter that corresponds to the ratio of True Positive (TP) predictions and the sum of TP and False Positive (FP) predictions. Recall is the ratio of TP and the sum of TP and False Negatives (FN). The method to decide whether a prediction is positive, or negative is based on the Intersection over Union (IoU). IoU is the ratio between the intersection between the predicted shape area and the ground truth shape area divided by the sum of the area of those shapes. The Average Precision score is computed

automatically for each class at different IoU thresholds, commonly at 0.5, 0.75 and 0.95 and then averaged to obtain the global mAP and for each class (Ghorbanzadeh et al., 2019; MAY 6 & Read, 2020).

Text S2. Facebook AI Research's Detectron2

Detectron2 is a library developed by the Facebook AI Research team, and is an evolution of Detectron library (Wu et al., 2019a, 2020) and maskrcnn-benchmark (Massa & Girshick, 2018) Detectron2's developers provide several models such as Faster- and Mask- Region-based Convolutional Neural Network (Faster-RCNN, Mask R-CNN), RetinaNet, DensePose, Cascade R-CNN, Panoptic FPN, and TensorMask, including their relative baseline pre-trained versions (Wu et al., 2019b) which can be used to further train custom models.

All of these are state-of-the-art trained architectures specialized in object detection, image segmentation, instance segmentation and pose estimation. Moreover, this library is well documented (Facebook AI Research, 2020) and the code is maintained periodically, including features updates and integrations of newer models (Wu et al., 2019b). Considering all these features, Detectron2 has been chosen as a core library to develop new tools for planetary mapper. Pytorch has been used as a framework (Paszke et al., 2019).

All included pre-trained models are compatible with the tool presented in this work, but for the specific task of instance segmentation for mapping landforms, the Mask R-CNN networks have been considered the defaults since are specific for object instance segmentation tasks (He et al., 2018).

Text S3. Deep Learning main workflow steps

Depending on the data size and format, the labelling software and the DeepLearning architecture and approach, may vary slightly. Common data pre-processing includes a data format conversion from the source data format to a lighter format compatible with both the labelling tool and the Deep Learning tool.

Common file formats include jpeg, png and tiff, while the file size is usually lower than 1024 x 1024 pixel.

To meet those requirements, images can be resized, loosing spatial resolution, cropped, loosing portion of the image and tiled, increasing the number of the images.

For instance, in this work have been used Reduced Data Record (RDR) RED channel data acquired by the High-Resolution Imaging Science Experiment (HiRISE) on board the Mars Reconnaissance Orbiter (MRO) and consist of calibrated and map-projected images at highest spatial resolution possible, provided in JPEG2000 (JP2) file format. File size of these images may reach few Gigabytes with used

Data are then ingested in labeling tool that produce ancillary data containing all the labels in a format compatible with the Deep Learning training pipeline. For Object Detection, labels consist of bounding boxes containing a single object of interest, while for Instance Segmentation, labels consist of polygonal shape containing a single object of interest. For both types of labels, a single class category must be assigned.

Before of within the training pipeline, the source dataset is divided into three main sub-datasets: train, test and valid, with a common rule-of-thumb proportion of 70:20:10%, meaning that 70% of the data will be used for train dataset, 20% for the test dataset and 10% for validating the trained model.

Train and test dataset are then used in the training pipeline, in which the test dataset is used for evaluating the model while training.

After the completion of the training, the model is evaluated using the valid dataset, to assess how it performs with unseen data.

Text S4. Image masks

The filters that are used to create masks can be based on both users defined custom values or no-data values embedded in image's metadata. For instance, some images may have Not-a-Number (NaN) values as no-data, while others may have other fixed values that are commonly provided in dataset ancillary files if not embedded in the data.

Segmentation results of Mask R-CNNs have instance masks as results that can cover the whole image (image segmentation) or only identified objects (instance segmentation) as shown in Figure S1.

Text S5. Docker-compose and dockerfiles

The major advantage of usage of docker platform resides in the capabilities of running services in an instantiated environment, independent from the host operating system without worrying of library dependencies, compilers, interpreters and so on, thus providing great cross-platform compatibility. Moreover, docker containers can be shared both as pre-built container images for fast deployment and as a docker building recipe named dockerfile. Those recipes can be customized by combining with other dockerfiles and, or, with pre-build docker images. Dockerfiles can also be used in combination with docker-compose (Merkel, 2014), a tool for running multi-container Docker applications. DeepLandforms repository (Nodjoumi, 2021) contains both single separate dockerfiles and a docker-compose configuration files for automatic building of the necessary docker images with only minor configuration requirements by the user. These files are available both in Github repository (Nodjoumi, 2021) and Zenodo (Nodjoumi, 2021).

The repository is structured as follows:

- Dockerfiles for creating the main tool docker images containing training and inference jupyter notebooks,
- Dockerfile for creating tensorboard docker image, an open-source tool for monitoring model training [81],
- Dockerfile for creating labelme docker image, an open-source tool for image polygonal annotation in Common Object Context (COCO) label format (Lin et al., 2015),
- Dockerfile for creating ImageProcessingUtils docker image, an open-source tool for image resizing and tiles,
- A folder containing all the developed notebooks and addons,

- README, containing brief description and initial guidelines.

Text S6. DeepLandforms Notebooks

DeepLandforms-Training notebook is an implementation of the Detectron2 Library's training components in a jupyter notebook, in which is possible to control all the main hyperparameters mentioned in Text S1, such as Epochs, LearningRate, batch size and more, and other parameters such the percentage used to create the train, test, and valid datasets.

The notebook automatically creates such datasets and visualize pie-charts representing each dataset with class distributions.

After dataset creation the notebook create an ancillary file containing all the classes that has been trained and save it in the same directory of the trained model.

DeepLandforms-Segmentation notebook is an implementation of the Detectron2 Library's inference components. This notebook includes several custom functions which are used to compute the world coordinates of the detection masks and their conversion into vectorial data, including geopackage creation. Moreover, a specific function has been developed to convert the detection masks into label files in COCO json format that can be directly used to perform new training sessions.

Text S7. Mask_rcnn_R_50_FPN model configuration

This model configuration can be visualized by using the following lines of code after loading properly the corresponding configuration.

Python3 code:

```
from detectron2.engine import DefaultTrainer
trainer = DefaultTrainer(cfg)
trainer.resume_or_load(resume=False)
```

GeneralizedRCNN(

(backbone): FPN(

(fpn_lateral2): Conv2d(256, 256, kernel_size=(1, 1), stride=(1, 1))

(fpn_output2): Conv2d(256, 256, kernel_size=(3, 3), stride=(1, 1), padding=(1, 1))

(fpn_lateral3): Conv2d(512, 256, kernel_size=(1, 1), stride=(1, 1))

(fpn_output3): Conv2d(256, 256, kernel_size=(3, 3), stride=(1, 1), padding=(1, 1))

(fpn_lateral4): Conv2d(1024, 256, kernel_size=(1, 1), stride=(1, 1))

(fpn_output4): Conv2d(256, 256, kernel_size=(3, 3), stride=(1, 1), padding=(1, 1))

(fpn_lateral5): Conv2d(2048, 256, kernel_size=(1, 1), stride=(1, 1))

(fpn_output5): Conv2d(256, 256, kernel_size=(3, 3), stride=(1, 1), padding=(1, 1))

(top_block): LastLevelMaxPool()

(bottom_up): ResNet(

(stem): BasicStem(

(conv1): Conv2d(

```

3, 64, kernel_size=(7, 7), stride=(2, 2), padding=(3, 3), bias=False
(norm): FrozenBatchNorm2d(num_features=64, eps=1e-05)
)
)
(res2): Sequential(
(0): BottleneckBlock(
(shortcut): Conv2d(
64, 256, kernel_size=(1, 1), stride=(1, 1), bias=False
(norm): FrozenBatchNorm2d(num_features=256, eps=1e-05)
)
(conv1): Conv2d(
64, 64, kernel_size=(1, 1), stride=(1, 1), bias=False
(norm): FrozenBatchNorm2d(num_features=64, eps=1e-05)
)
(conv2): Conv2d(
64, 64, kernel_size=(3, 3), stride=(1, 1), padding=(1, 1), bias=False
(norm): FrozenBatchNorm2d(num_features=64, eps=1e-05)
)
(conv3): Conv2d(
64, 256, kernel_size=(1, 1), stride=(1, 1), bias=False
(norm): FrozenBatchNorm2d(num_features=256, eps=1e-05)
)
)
(1): BottleneckBlock(
(conv1): Conv2d(
256, 64, kernel_size=(1, 1), stride=(1, 1), bias=False
(norm): FrozenBatchNorm2d(num_features=64, eps=1e-05)
)
(conv2): Conv2d(
64, 64, kernel_size=(3, 3), stride=(1, 1), padding=(1, 1), bias=False
(norm): FrozenBatchNorm2d(num_features=64, eps=1e-05)
)
(conv3): Conv2d(
64, 256, kernel_size=(1, 1), stride=(1, 1), bias=False
(norm): FrozenBatchNorm2d(num_features=256, eps=1e-05)
)
)
(2): BottleneckBlock(
(conv1): Conv2d(
256, 64, kernel_size=(1, 1), stride=(1, 1), bias=False
(norm): FrozenBatchNorm2d(num_features=64, eps=1e-05)
)
(conv2): Conv2d(
64, 64, kernel_size=(3, 3), stride=(1, 1), padding=(1, 1), bias=False
(norm): FrozenBatchNorm2d(num_features=64, eps=1e-05)
)
(conv3): Conv2d(

```

```

64, 256, kernel_size=(1, 1), stride=(1, 1), bias=False
(norm): FrozenBatchNorm2d(num_features=256, eps=1e-05)
)
)
)
(res3): Sequential(
(0): BottleneckBlock(
(shortcut): Conv2d(
256, 512, kernel_size=(1, 1), stride=(2, 2), bias=False
(norm): FrozenBatchNorm2d(num_features=512, eps=1e-05)
)
(conv1): Conv2d(
256, 128, kernel_size=(1, 1), stride=(2, 2), bias=False
(norm): FrozenBatchNorm2d(num_features=128, eps=1e-05)
)
(conv2): Conv2d(
128, 128, kernel_size=(3, 3), stride=(1, 1), padding=(1, 1), bias=False
(norm): FrozenBatchNorm2d(num_features=128, eps=1e-05)
)
(conv3): Conv2d(
128, 512, kernel_size=(1, 1), stride=(1, 1), bias=False
(norm): FrozenBatchNorm2d(num_features=512, eps=1e-05)
)
)
)
(1): BottleneckBlock(
(conv1): Conv2d(
512, 128, kernel_size=(1, 1), stride=(1, 1), bias=False
(norm): FrozenBatchNorm2d(num_features=128, eps=1e-05)
)
(conv2): Conv2d(
128, 128, kernel_size=(3, 3), stride=(1, 1), padding=(1, 1), bias=False
(norm): FrozenBatchNorm2d(num_features=128, eps=1e-05)
)
(conv3): Conv2d(
128, 512, kernel_size=(1, 1), stride=(1, 1), bias=False
(norm): FrozenBatchNorm2d(num_features=512, eps=1e-05)
)
)
)
(2): BottleneckBlock(
(conv1): Conv2d(
512, 128, kernel_size=(1, 1), stride=(1, 1), bias=False
(norm): FrozenBatchNorm2d(num_features=128, eps=1e-05)
)
(conv2): Conv2d(
128, 128, kernel_size=(3, 3), stride=(1, 1), padding=(1, 1), bias=False
(norm): FrozenBatchNorm2d(num_features=128, eps=1e-05)
)
)
)

```

```

(conv3): Conv2d(
  128, 512, kernel_size=(1, 1), stride=(1, 1), bias=False
  (norm): FrozenBatchNorm2d(num_features=512, eps=1e-05)
)
)
(3): BottleneckBlock(
  (conv1): Conv2d(
    512, 128, kernel_size=(1, 1), stride=(1, 1), bias=False
    (norm): FrozenBatchNorm2d(num_features=128, eps=1e-05)
  )
  (conv2): Conv2d(
    128, 128, kernel_size=(3, 3), stride=(1, 1), padding=(1, 1), bias=False
    (norm): FrozenBatchNorm2d(num_features=128, eps=1e-05)
  )
  (conv3): Conv2d(
    128, 512, kernel_size=(1, 1), stride=(1, 1), bias=False
    (norm): FrozenBatchNorm2d(num_features=512, eps=1e-05)
  )
)
)
(res4): Sequential(
  (0): BottleneckBlock(
    (shortcut): Conv2d(
      512, 1024, kernel_size=(1, 1), stride=(2, 2), bias=False
      (norm): FrozenBatchNorm2d(num_features=1024, eps=1e-05)
    )
    (conv1): Conv2d(
      512, 256, kernel_size=(1, 1), stride=(2, 2), bias=False
      (norm): FrozenBatchNorm2d(num_features=256, eps=1e-05)
    )
    (conv2): Conv2d(
      256, 256, kernel_size=(3, 3), stride=(1, 1), padding=(1, 1), bias=False
      (norm): FrozenBatchNorm2d(num_features=256, eps=1e-05)
    )
    (conv3): Conv2d(
      256, 1024, kernel_size=(1, 1), stride=(1, 1), bias=False
      (norm): FrozenBatchNorm2d(num_features=1024, eps=1e-05)
    )
  )
  (1): BottleneckBlock(
    (conv1): Conv2d(
      1024, 256, kernel_size=(1, 1), stride=(1, 1), bias=False
      (norm): FrozenBatchNorm2d(num_features=256, eps=1e-05)
    )
    (conv2): Conv2d(
      256, 256, kernel_size=(3, 3), stride=(1, 1), padding=(1, 1), bias=False
      (norm): FrozenBatchNorm2d(num_features=256, eps=1e-05)

```

```

)
(conv3): Conv2d(
  256, 1024, kernel_size=(1, 1), stride=(1, 1), bias=False
  (norm): FrozenBatchNorm2d(num_features=1024, eps=1e-05)
)
)
(2): BottleneckBlock(
  (conv1): Conv2d(
    1024, 256, kernel_size=(1, 1), stride=(1, 1), bias=False
    (norm): FrozenBatchNorm2d(num_features=256, eps=1e-05)
  )
  (conv2): Conv2d(
    256, 256, kernel_size=(3, 3), stride=(1, 1), padding=(1, 1), bias=False
    (norm): FrozenBatchNorm2d(num_features=256, eps=1e-05)
  )
  (conv3): Conv2d(
    256, 1024, kernel_size=(1, 1), stride=(1, 1), bias=False
    (norm): FrozenBatchNorm2d(num_features=1024, eps=1e-05)
  )
)
(3): BottleneckBlock(
  (conv1): Conv2d(
    1024, 256, kernel_size=(1, 1), stride=(1, 1), bias=False
    (norm): FrozenBatchNorm2d(num_features=256, eps=1e-05)
  )
  (conv2): Conv2d(
    256, 256, kernel_size=(3, 3), stride=(1, 1), padding=(1, 1), bias=False
    (norm): FrozenBatchNorm2d(num_features=256, eps=1e-05)
  )
  (conv3): Conv2d(
    256, 1024, kernel_size=(1, 1), stride=(1, 1), bias=False
    (norm): FrozenBatchNorm2d(num_features=1024, eps=1e-05)
  )
)
(4): BottleneckBlock(
  (conv1): Conv2d(
    1024, 256, kernel_size=(1, 1), stride=(1, 1), bias=False
    (norm): FrozenBatchNorm2d(num_features=256, eps=1e-05)
  )
  (conv2): Conv2d(
    256, 256, kernel_size=(3, 3), stride=(1, 1), padding=(1, 1), bias=False
    (norm): FrozenBatchNorm2d(num_features=256, eps=1e-05)
  )
  (conv3): Conv2d(
    256, 1024, kernel_size=(1, 1), stride=(1, 1), bias=False
    (norm): FrozenBatchNorm2d(num_features=1024, eps=1e-05)
  )
)

```

```

)
(5): BottleneckBlock(
  (conv1): Conv2d(
    1024, 256, kernel_size=(1, 1), stride=(1, 1), bias=False
    (norm): FrozenBatchNorm2d(num_features=256, eps=1e-05)
  )
  (conv2): Conv2d(
    256, 256, kernel_size=(3, 3), stride=(1, 1), padding=(1, 1), bias=False
    (norm): FrozenBatchNorm2d(num_features=256, eps=1e-05)
  )
  (conv3): Conv2d(
    256, 1024, kernel_size=(1, 1), stride=(1, 1), bias=False
    (norm): FrozenBatchNorm2d(num_features=1024, eps=1e-05)
  )
)
)
)
(res5): Sequential(
  (0): BottleneckBlock(
    (shortcut): Conv2d(
      1024, 2048, kernel_size=(1, 1), stride=(2, 2), bias=False
      (norm): FrozenBatchNorm2d(num_features=2048, eps=1e-05)
    )
    (conv1): Conv2d(
      1024, 512, kernel_size=(1, 1), stride=(2, 2), bias=False
      (norm): FrozenBatchNorm2d(num_features=512, eps=1e-05)
    )
    (conv2): Conv2d(
      512, 512, kernel_size=(3, 3), stride=(1, 1), padding=(1, 1), bias=False
      (norm): FrozenBatchNorm2d(num_features=512, eps=1e-05)
    )
    (conv3): Conv2d(
      512, 2048, kernel_size=(1, 1), stride=(1, 1), bias=False
      (norm): FrozenBatchNorm2d(num_features=2048, eps=1e-05)
    )
  )
)
(1): BottleneckBlock(
  (conv1): Conv2d(
    2048, 512, kernel_size=(1, 1), stride=(1, 1), bias=False
    (norm): FrozenBatchNorm2d(num_features=512, eps=1e-05)
  )
  (conv2): Conv2d(
    512, 512, kernel_size=(3, 3), stride=(1, 1), padding=(1, 1), bias=False
    (norm): FrozenBatchNorm2d(num_features=512, eps=1e-05)
  )
  (conv3): Conv2d(
    512, 2048, kernel_size=(1, 1), stride=(1, 1), bias=False
    (norm): FrozenBatchNorm2d(num_features=2048, eps=1e-05)
  )
)

```



```

)
(box_predictor): FastRCNNOutputLayers(
  (cls_score): Linear(in_features=1024, out_features=8, bias=True)
  (bbox_pred): Linear(in_features=1024, out_features=28, bias=True)
)
(mask_pooler): ROIPooler(
  (level_poolers): ModuleList(
    (0): ROIAlign(output_size=(14, 14), spatial_scale=0.25, sampling_ratio=0, aligned=True)
    (1): ROIAlign(output_size=(14, 14), spatial_scale=0.125, sampling_ratio=0, aligned=True)
    (2): ROIAlign(output_size=(14, 14), spatial_scale=0.0625, sampling_ratio=0, aligned=True)
    (3): ROIAlign(output_size=(14, 14), spatial_scale=0.03125, sampling_ratio=0, aligned=True)
  )
)
(mask_head): MaskRCNNConvUpsampleHead(
  (mask_fcn1): Conv2d(
    256, 256, kernel_size=(3, 3), stride=(1, 1), padding=(1, 1)
  )
  (activation): ReLU()
)
(mask_fcn2): Conv2d(
    256, 256, kernel_size=(3, 3), stride=(1, 1), padding=(1, 1)
  )
  (activation): ReLU()
)
(mask_fcn3): Conv2d(
    256, 256, kernel_size=(3, 3), stride=(1, 1), padding=(1, 1)
  )
  (activation): ReLU()
)
(mask_fcn4): Conv2d(
    256, 256, kernel_size=(3, 3), stride=(1, 1), padding=(1, 1)
  )
  (activation): ReLU()
)
(deconv): ConvTranspose2d(256, 256, kernel_size=(2, 2), stride=(2, 2))
(deconv_relu): ReLU()
(predictor): Conv2d(256, 7, kernel_size=(1, 1), stride=(1, 1))
)
)
)
)

```

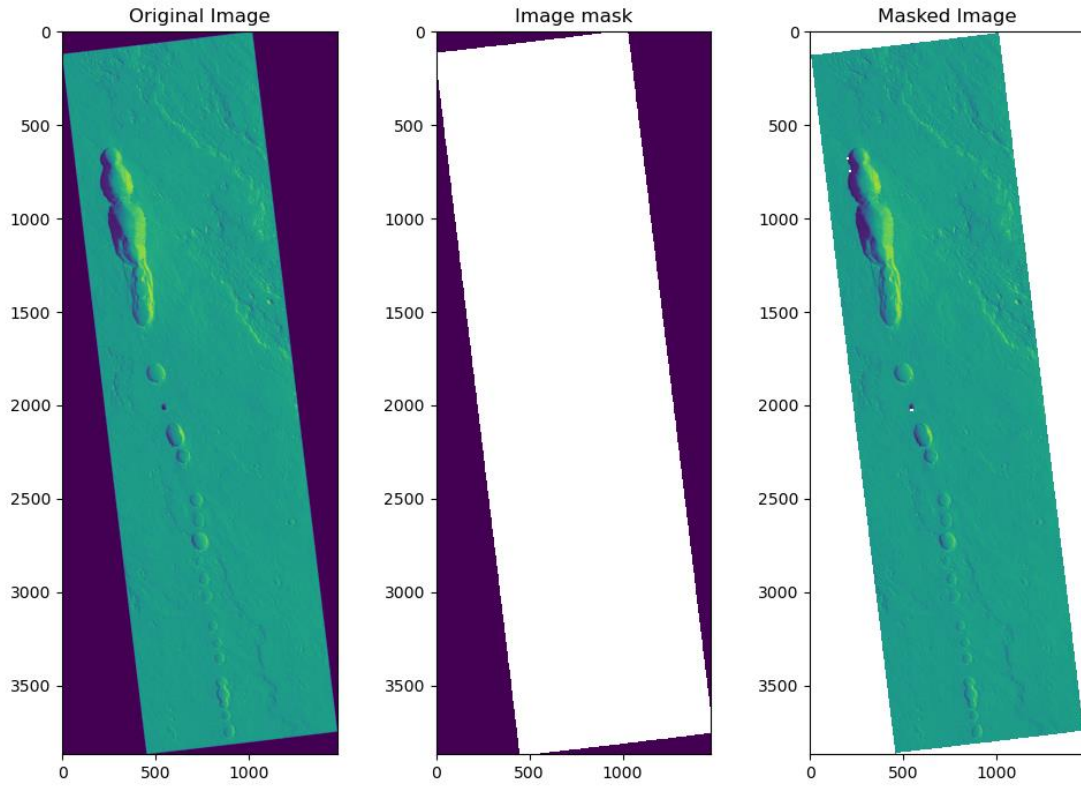


Figure S1. Example of masks on HiRISE image. Purple color represents nodata value.

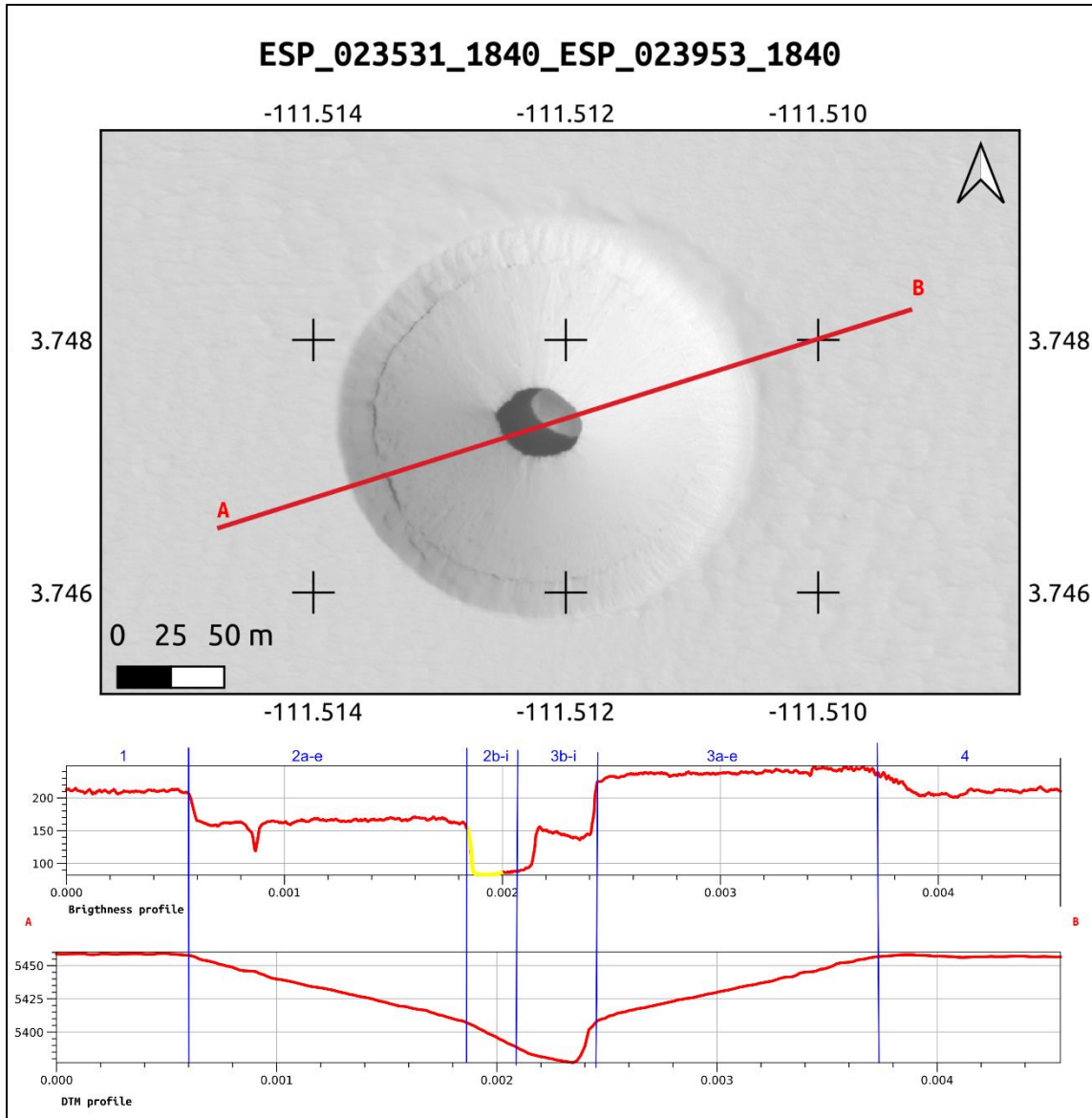


Figure S2 Comparison of brightness and DTM profiles for a Type-1 nested in Type-2 on ESP_23531-ESP_23953 stereo pair, red channel. In blue, an attempt to identify the correspondence of the brightness sections on a DTM derived from photogrammetry of HiRISE stereo pair. In yellow, the portion of the DTM profile interpolated by the Socet Set ((c) BAE Systems) software. This is due to lack of usable data in both the images processed using photogrammetry (*HiRISE / About HiRISE Digital Terrain Models, 2021*)

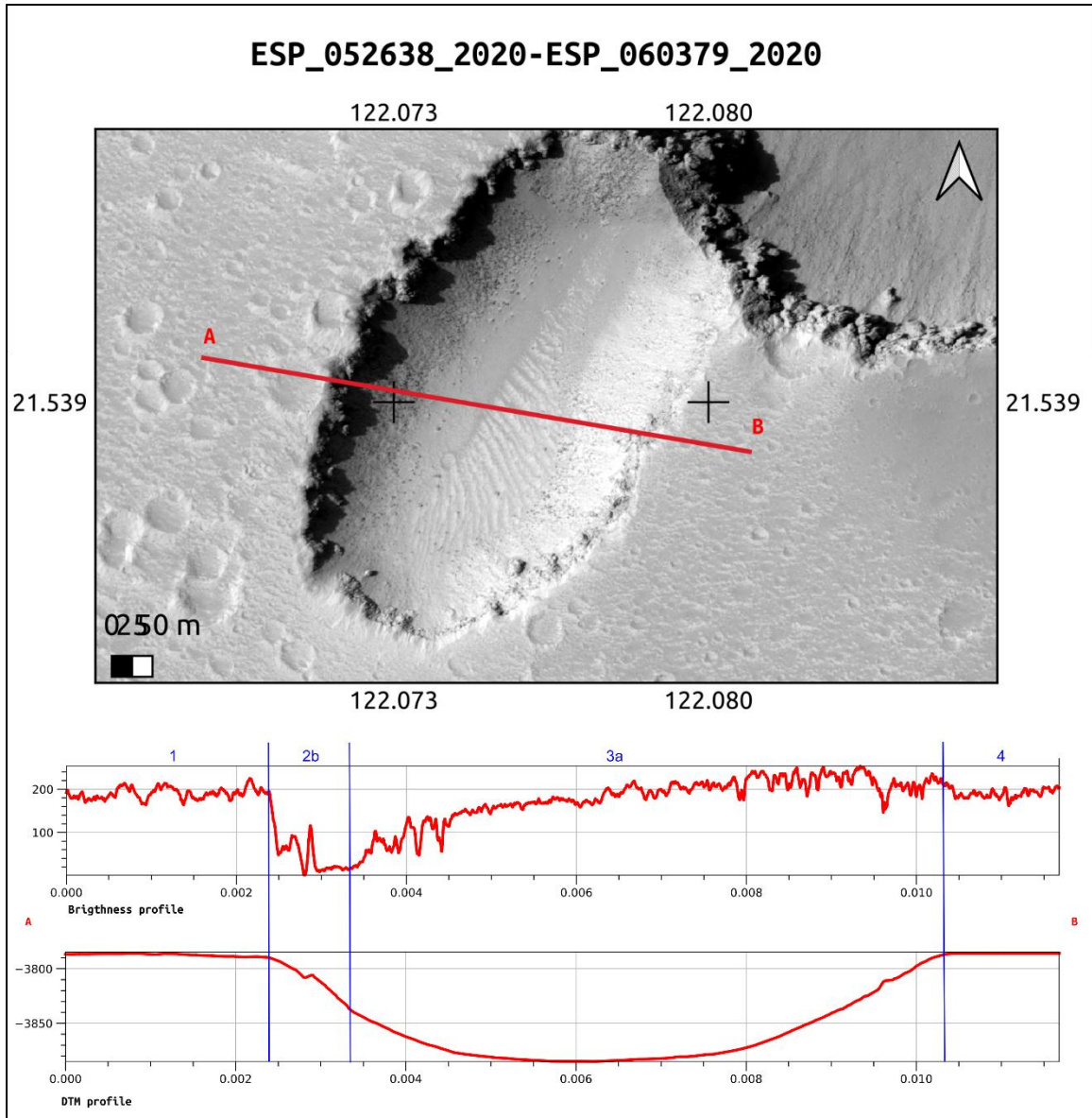


Figure S3. Comparison of brightness and DTM profiles for a Type-3 on ESP_23531_RED ortho image, the DTM is derived from ESP_23531-ESP_23953 stereo pair, red channel. In blue, an attempt to identify the correspondence of the brightness sections on a DTM derived from photogrammetry of HiRISE stereo pair. In yellow, the portion of the DTM profile interpolated by the Socet Set ((c) BAE Systems) software. This is due to lack of usable data in both the images processed using photogrammetry (*HiRISE / About HiRISE Digital Terrain Models, 2021*)

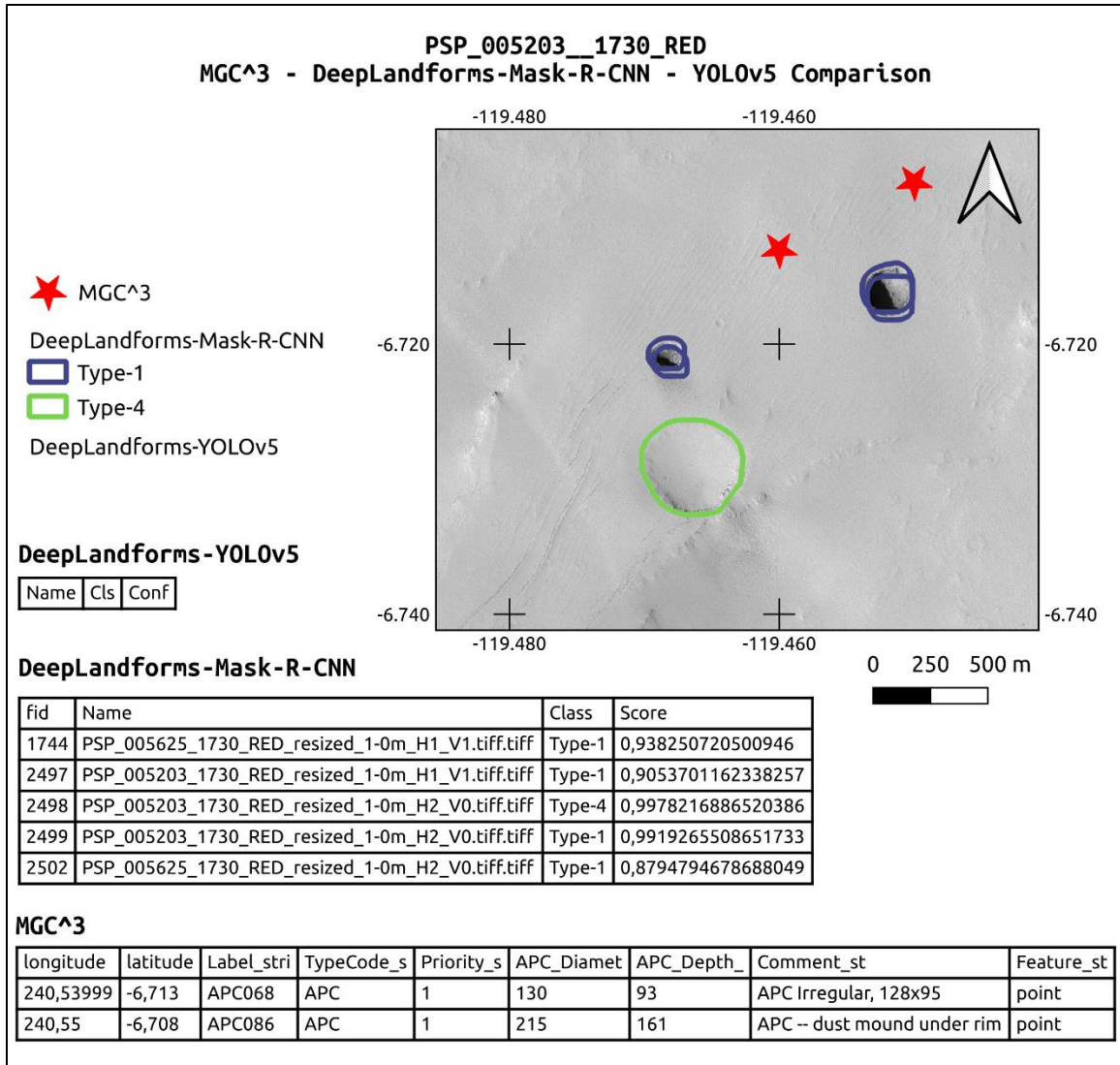


Figure S4. Example of multiple polygons, slightly mis-aligned, detected on multiple images acquired of the same area compared to entries of the MGC^3 database with both attribute tables displayed. The results, stored in a geopackage, were opened in a GIS environment where can be styled using different colors for each class. The offset of MGC^3 points is probably caused by the coordinate conversion of the source MGC^3 csv file into shapefile.

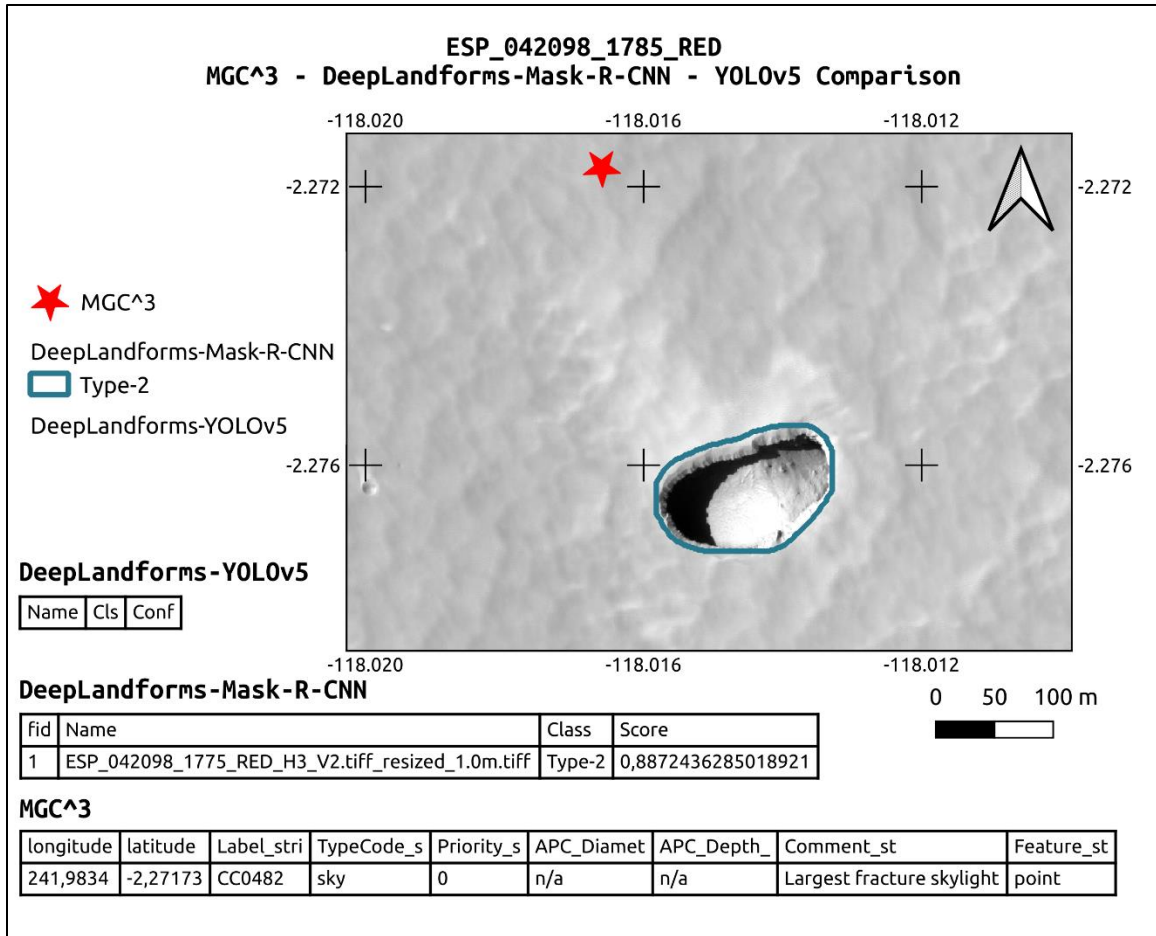


Figure S5. Example of detection on HiRISE Red channel image and comparison between MGC^3, DeepLandforms-YOLOv5 object detection and DeepLandforms-Mask-R-CNN instance segmentation. In this case Mask-R-CNN has difficulties to classify since the landform has properties similar to both Type-2, Type-1 and Type-3. Tables show attributes of fields in the shapefiles. The offset of MGC^3 points is probably caused by the coordinate conversion of the source MGC^3 csv file into shapefile.

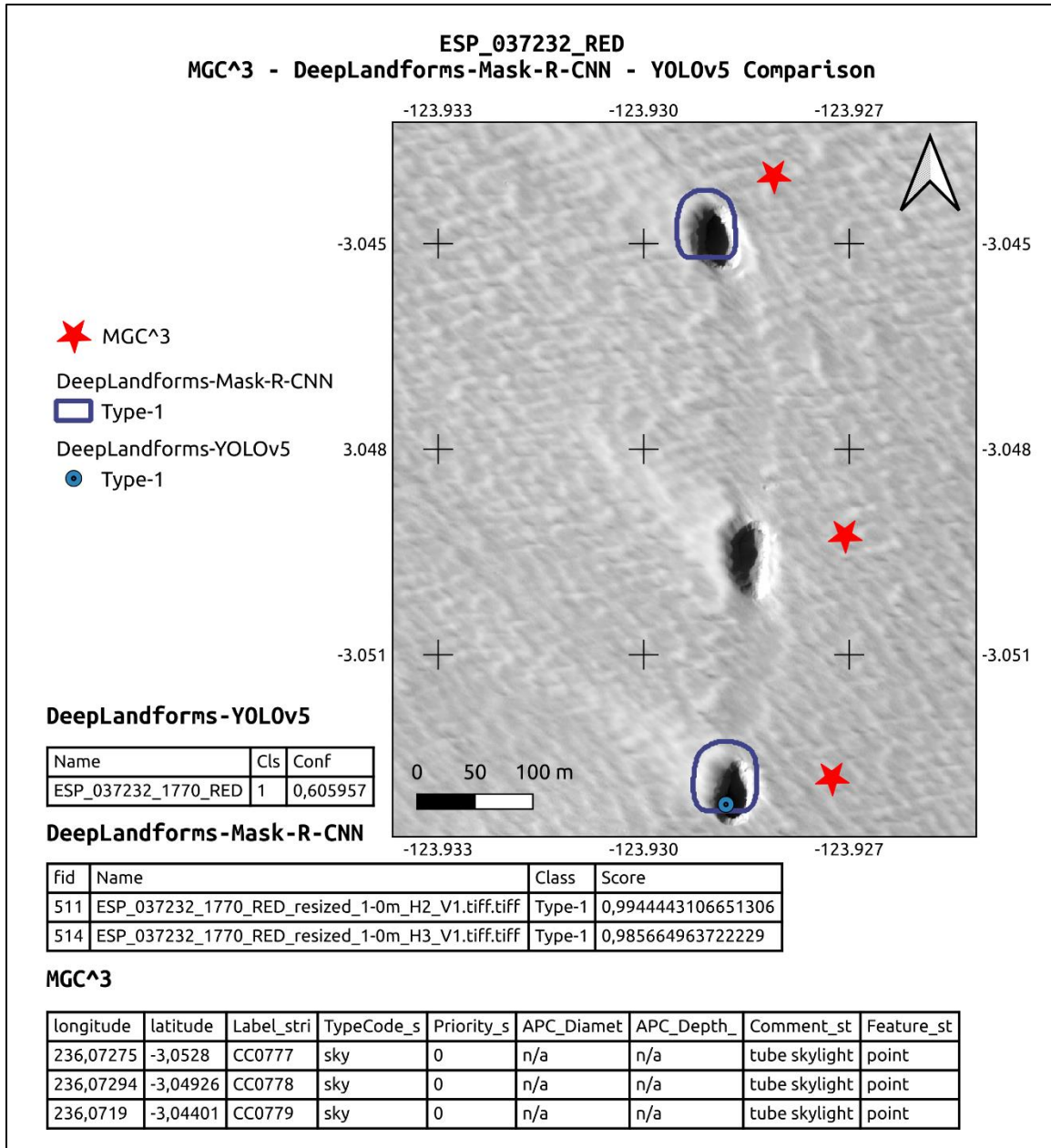


Figure S6. Example of detection on HiRISE Red channel image and comparison between MGC^3, DeepLandforms-YOLOv5 object detection and DeepLandforms-Mask-R-CNN instance segmentation. Tables show attributes of fields in the shapefiles. The offset of MGC^3 points is probably caused by the coordinate conversion of the source MGC^3 csv file into shapefile.

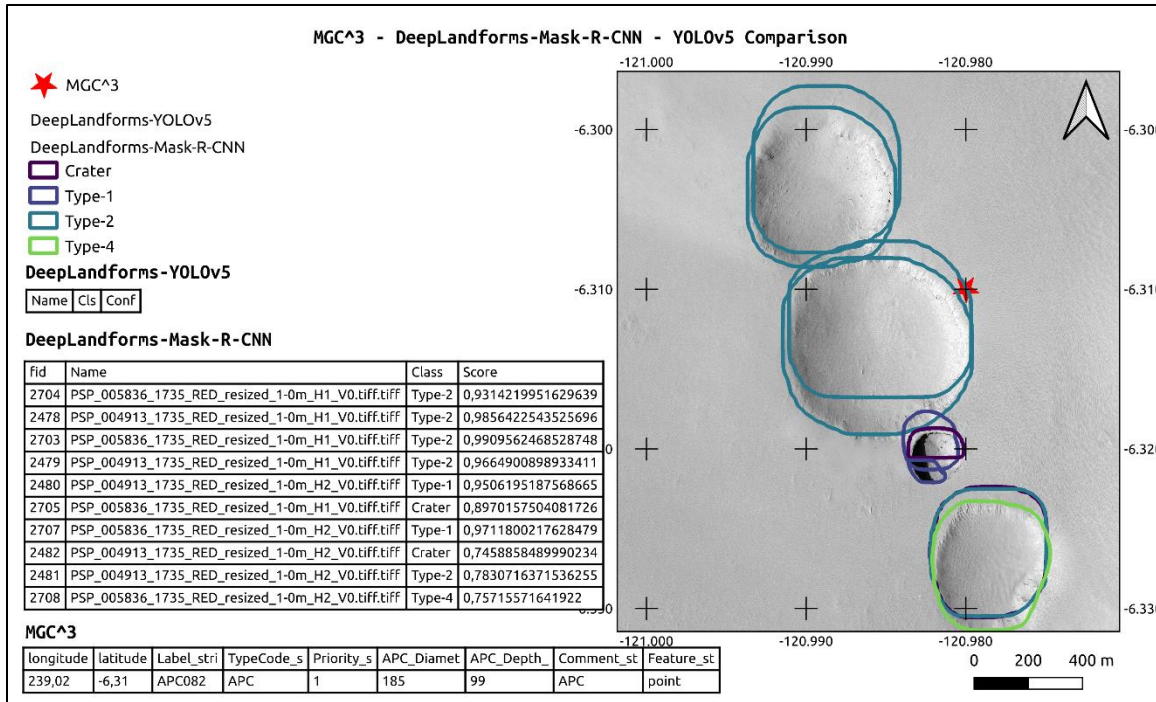


Figure S7. Example of detection on HiRISE Red channel image and comparison between MGC^3, DeepLandforms-YOLOv5 object detection and DeepLandforms-Mask-R-CNN instance segmentation. Multiple misclassification and segmentation error occurs. Classification errors, such as Type-1/Crater are mostly caused by the small training dataset. Segmentation errors are caused by both the small dataset and by inference performed on tiles. For instance, Type-1 and Type-2 have straight horizontal lines that correspond to the edge of the tile. This specific error can be mitigated by using larger tiles or by implementing a sliding-window analysis. Tables show attributes of fields in the shapefiles. The offset of MGC^3 points is probably caused by the coordinate conversion of the source MGC^3 csv file into shapefile.

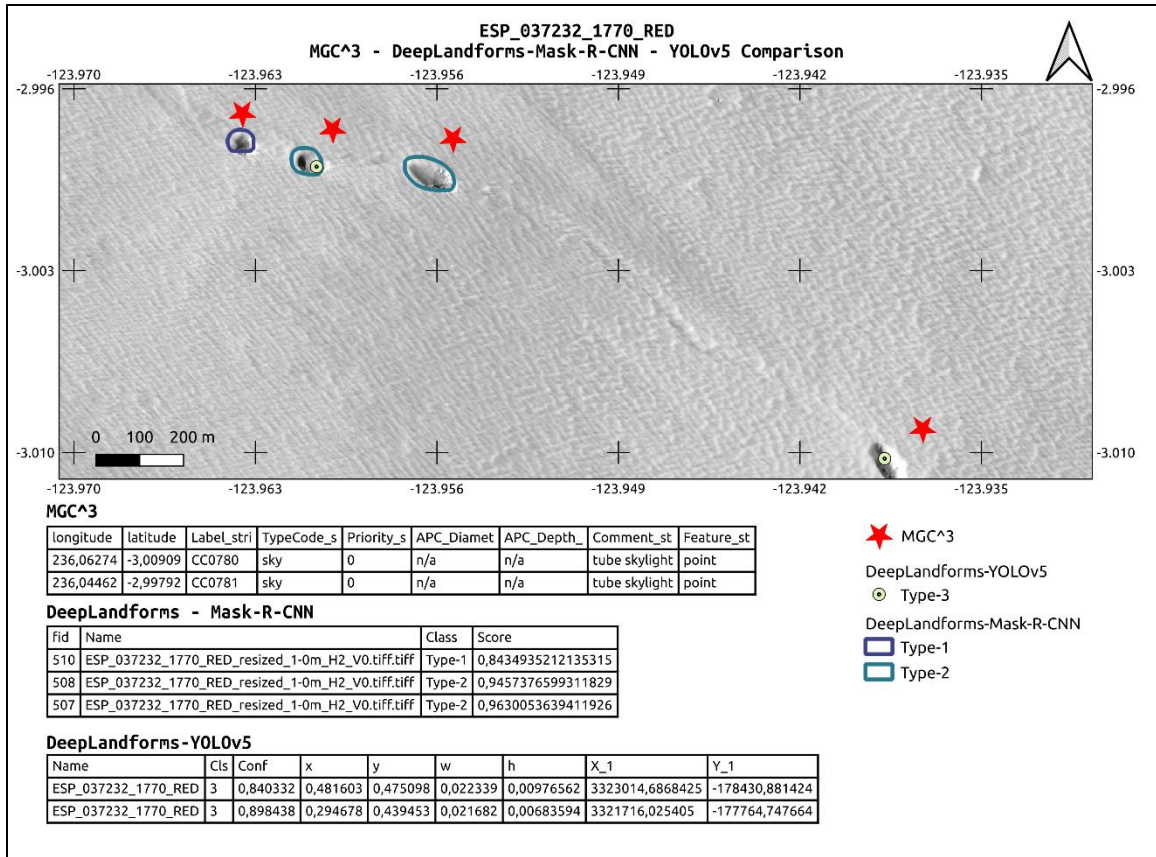


Figure S8. Example of detections on full HiRISE Red channel image. The first two shapes on top, present segmentation, and classification errors due to the inference that was performed on tiles instead of the full image. Other shapes present misclassification errors mostly due to the very small training datasets. Tables show attributes of fields in the shapefiles. These landforms are not present in the MGC^3.

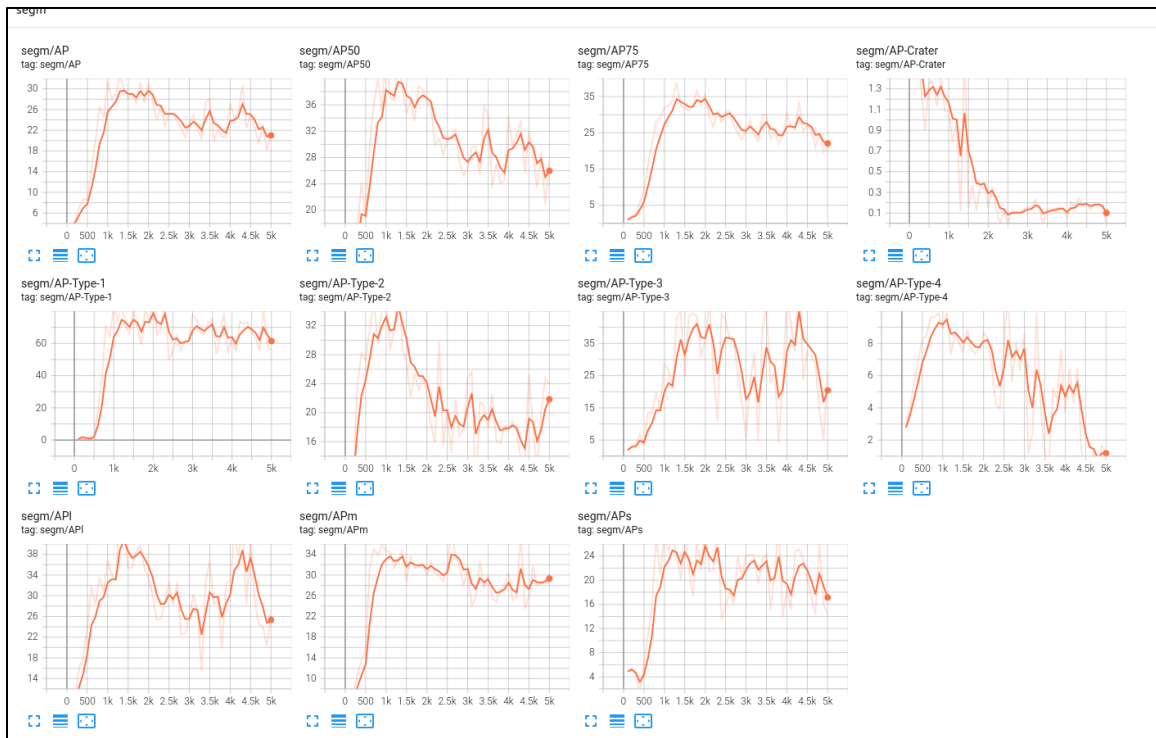


Figure S9. Mean Average Precision values for the object detection, shows an overall average value compared to the Detectron2's benchmarks (Wu et al., 2019b) except for Type-4 and Crater landforms.

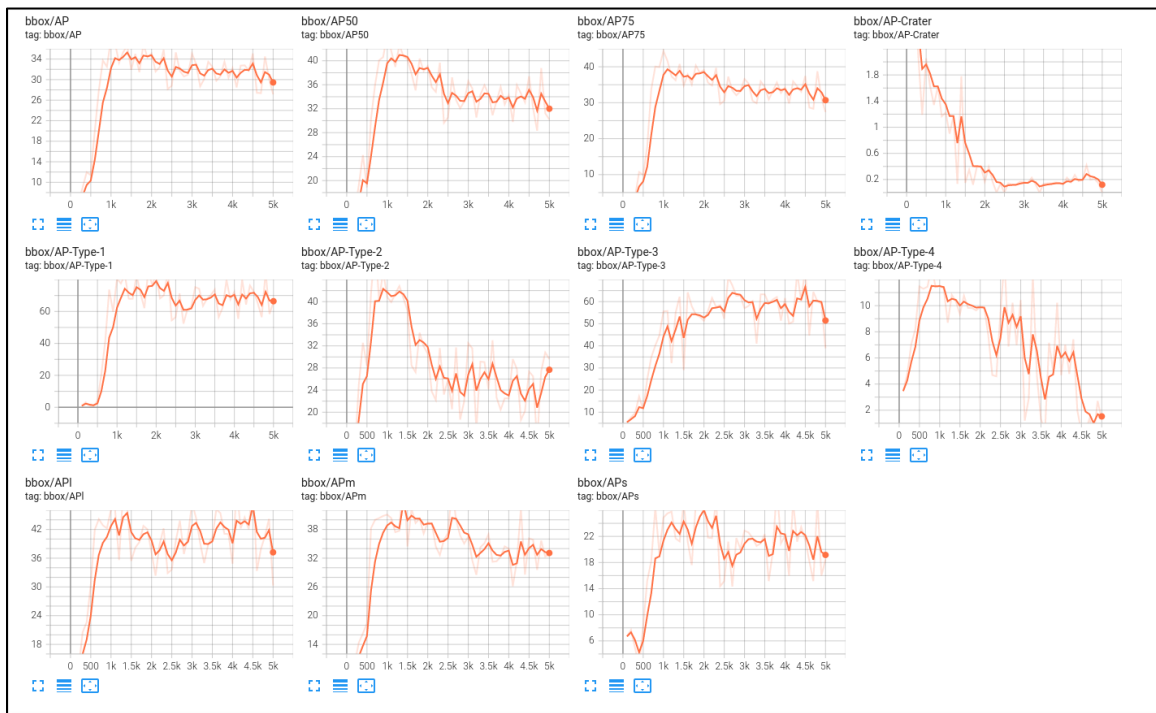


Figure S10. Mean Average Precision values for the segmentation, shows an overall average value compared to the Detectron2's benchmarks (Wu et al., 2019b) except for Type-4 and Crater landforms.

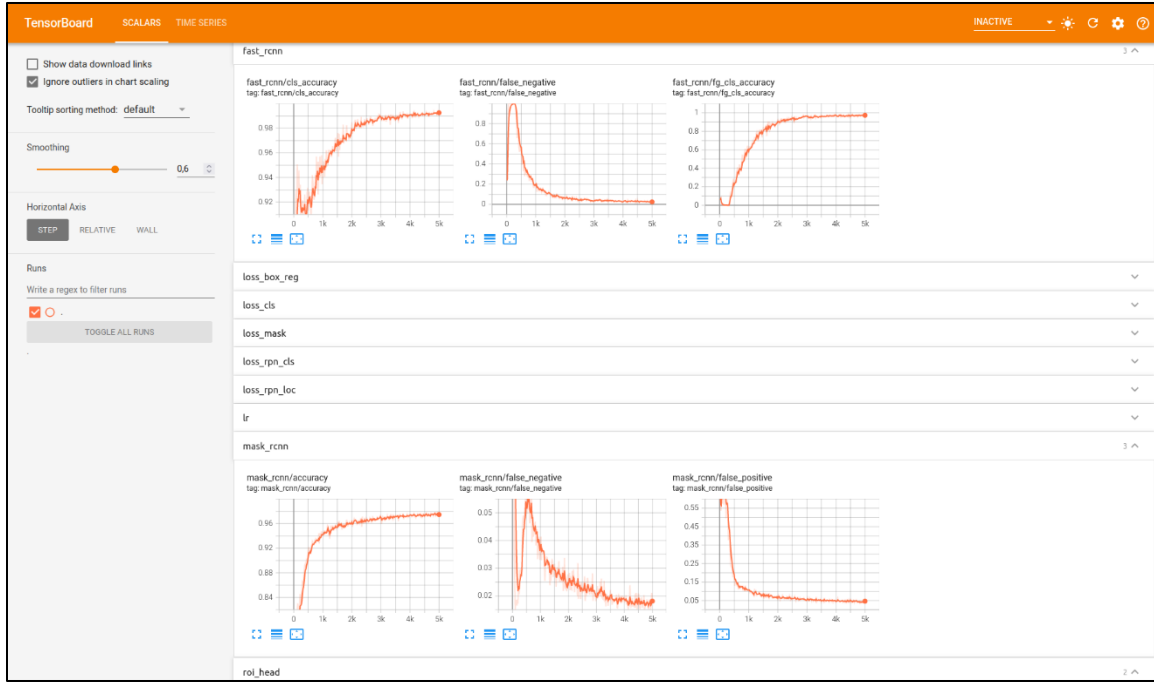


Figure S11. Overall training results for both object detection and instance segmentation visualized through *tensorboard* interface.

Parameter	Description
Shape	
Size	Width, Length
Height	Height
Texture	The frequency of tonal changes
Pattern	The spatial arrangement of objects or elements in a given area.
Tone/Hue	Black&White brightness and color hue, expression of the amount and type of light reflected (or emitted) by an object and reflection of the environmental condition during the acquisition
Location/Association	Spatial relations between an object and its surroundings

Table S1. Main parameters that describe a landform. (Tempfli et al., 2009).

Acronym	Meaning
AI	Artificial Intelligence
Cascade-R-CNN	Cascade Regional CNN
CNN	Convolutional Neural Network
COCO	Common Object Context
CTX	Context Camera
CUDA	Compute Unified Device Architecture
DEM	Digital Elevation Model
DL	Deep Learning
DN	Digital Numbers
DTM	Digital Terrain Model
EDR	Experiment Data Record
FN	False Negative
FP	False Positive
Faster-R-CNN	Faster Regional CNN
GDAL	Geospatial Data Abstraction Software Library
GIS	Geographic Information System
GPU	Graphical Processor Unit
HiRISE	High Resolution Imaging Science Experiment
ImS	Image Segmentation
InS	Instance Segmentation
LRO	Lunar Reconnaissance Orbiter
Mask-R-CNN	Mask Regional CNN
mAP	Mean Average Precision
ML	Machine Learning
MRO	Mars Reconnaissance Orbiter
NAC	Narrow Angle Camera
NIR	Near InfraRed
OD	Object Detection
ODE	Orbital Data Explorer
OGC	Open Geospatial Consortium
Panoptic FPN	Panoptic Feature Proposal Network
RAM	Random Access Memory
R-CNN	Regional CNN
RDR	Reduced Data Record
RetinaNet	RetinaNetwork
TP	True Positive
VIS	Visible
VRAM	Video RAM
WAC	Wide Angle Camera
YOLO	You Only Look Once

Table S2. List of main acronyms present in the main paper.

Parameter	Value
Epochs	1000 to 5000
Batch size	4 to 8
LearningRate	0,00025 to 0,002

Table S3. Ranges of parameters used in all training tests.

Type	Detection mAP	Segmentation mAP
Global	32	30
Type-1	65	55
Type-2	29	23
Type-3	38	25
Type-4	1	1
Crater	1	1

Table S4. Mean mAP obtained at the end of the training.

HiRISE RDR ODE-PDS Filename
ESP_012600_1655_RED.JP2
ESP_013167_1785_RED.JP2
ESP_013589_1785_RED.JP2
ESP_013681_1765_RED.JP2
ESP_013879_1720_RED.JP2
ESP_014077_1660_RED.JP2
ESP_014380_1775_RED.JP2
ESP_016213_1720_RED.JP2
ESP_016305_2265_RED.JP2
ESP_016411_1605_RED.JP2
ESP_016767_1785_RED.JP2
ESP_016978_1730_RED.JP2
ESP_017057_1715_RED.JP2
ESP_017202_1685_RED.JP2
ESP_019259_1715_RED.JP2
ESP_019272_1980_RED.JP2
ESP_019351_1795_RED.JP2
ESP_019852_1810_RED.JP2
ESP_019957_2220_RED.JP2

ESP_019984_1795_RED.JP2
ESP_019997_1975_RED.JP2
ESP_020246_2185_RED.JP2
ESP_021738_1625_RED.JP2
ESP_022661_1705_RED.JP2
ESP_023531_1840_RED.JP2
ESP_024481_1605_RED.JP2
ESP_024929_1720_RED.JP2
ESP_025892_1780_RED.JP2
ESP_026695_2020_RED.JP2
ESP_026907_1705_RED.JP2
ESP_028370_2215_RED.JP2
ESP_028450_1730_RED.JP2
ESP_028700_2085_RED.JP2
ESP_028793_1655_RED.JP2
ESP_035254_1585_RED.JP2
ESP_035478_1775_RED.JP2
ESP_037086_2025_RED.JP2
ESP_037232_1770_RED.JP2
ESP_041030_1735_RED.JP2
ESP_041162_1665_RED.JP2
ESP_041373_1660_RED.JP2
ESP_041900_1805_RED.JP2
ESP_042019_1730_RED.JP2
ESP_042085_1795_RED.JP2
ESP_042098_1775_RED.JP2
ESP_042678_1935_RED.JP2
ESP_043021_1775_RED.JP2
ESP_043153_1685_RED.JP2
ESP_043166_1775_RED.JP2
ESP_043974_2090_RED.JP2
ESP_044326_2045_RED.JP2
ESP_045830_1735_RED.JP2
ESP_045870_1650_RED.JP2
ESP_045975_1685_RED.JP2
ESP_046687_1725_RED.JP2
ESP_046964_1665_RED.JP2
ESP_049812_1735_RED.JP2
ESP_050234_1735_RED.JP2
ESP_050300_1735_RED.JP2

ESP_050379_1725_RED.JP2
ESP_052858_1595_RED.JP2
ESP_054703_2225_RED.JP2
ESP_055614_1605_RED.JP2
ESP_055811_2035_RED.JP2
ESP_056867_1695_RED.JP2
ESP_057025_1640_RED.JP2
ESP_057434_1790_RED.JP2
ESP_057777_1790_RED.JP2
ESP_058133_1770_RED.JP2
ESP_058186_1660_RED.JP2
ESP_058489_1785_RED.JP2
ESP_058542_1625_RED.JP2
ESP_059043_1610_RED.JP2
ESP_059544_1650_RED.JP2
ESP_059623_1790_RED.JP2
ESP_059702_1790_RED.JP2
ESP_061680_1985_RED.JP2
PSP_003647_1745_RED.JP2
PSP_004847_1745_RED.JP2
PSP_004913_1735_RED.JP2
PSP_005058_1720_RED.JP2
PSP_005203_1730_RED.JP2
PSP_005414_1735_RED.JP2
PSP_005625_1730_RED.JP2
PSP_005770_1745_RED.JP2
PSP_007022_2175_RED.JP2
PSP_009620_1660_RED.JP2
PSP_009712_1785_RED.JP2
PSP_009910_1690_RED.JP2

Table S5. List of source images used, available at (PDS Geosciences Nodes, 2020)

References

- Amazon Machine Learning. (2021). *Model Fit: Underfitting vs. Overfitting—Amazon Machine Learning*.
<https://docs.aws.amazon.com/machine-learning/latest/dg/model-fit-underfitting-vs-overfitting.html>
- Chen, X., Girshick, R., He, K., & Dollar, P. (2019). TensorMask: A foundation for dense object segmentation. *Proceedings of the IEEE International Conference on Computer Vision, 2019-October*, 2061–2069. <https://doi.org/10.1109/ICCV.2019.00215>
- Deng, J., Dong, W., Socher, R., Li, L.-J., Li, K., & Fei-Fei, L. (2009). Imagenet: A large-scale hierarchical image database. *2009 IEEE Conference on Computer Vision and Pattern Recognition*, 248–255.
- Dhillon, A., & Verma, G. K. (2020). Convolutional neural network: A review of models, methodologies and applications to object detection. *Progress in Artificial Intelligence*, 9(2), 85–112.
- Facebook AI Research. (2020). *Welcome to detectron2's documentation! —Detectron2 0.4.1 documentation*.
<https://detectron2.readthedocs.io/en/latest/index.html>
- Ghorbanzadeh, O., Blaschke, T., Gholamnia, K., Meena, S., Tiede, D., & Aryal, J. (2019). Evaluation of Different Machine Learning Methods and Deep-Learning Convolutional Neural Networks for Landslide Detection. *Remote Sensing*, 11(2), 196.
<https://doi.org/10.3390/rs11020196>
- Girshick, R. (2015). Fast r-cnn. *Proceedings of the IEEE International Conference on Computer Vision*, 1440–1448.
- Google Developers. (2021). *Reducing Loss: Learning Rate | Machine Learning Crash Course*. Google Developers.
<https://developers.google.com/machine-learning/crash-course/reducing-loss/learning-rate?hl=it>
- Gu, J., Wang, Z., Kuen, J., Ma, L., Shahroudy, A., Shuai, B., Liu, T., Wang, X., Wang, G., Cai, J., & Chen, T. (2018). Recent advances in convolutional neural networks. *Pattern Recognition*. <https://doi.org/10.1016/j.patcog.2017.10.013>
- He, K., Gkioxari, G., Dollár, P., & Girshick, R. (2018). Mask R-CNN. *ArXiv:1703.06870 [Cs]*. <http://arxiv.org/abs/1703.06870>
- HiRISE | About HiRISE Digital Terrain Models. (2021). <https://www.uahirise.org/dtm/about.php>
- Hoeser, T., & Kuenzer, C. (2020). Object detection and image segmentation with deep learning on Earth observation data: A review—part I: Evolution and recent trends. *Remote Sensing*, 12(10). <https://doi.org/10.3390/rs12101667>
- Howard, A. G., Zhu, M., Chen, B., Kalenichenko, D., Wang, W., Weyand, T., Andreetto, M., & Adam, H. (2017). MobileNets: Efficient Convolutional Neural Networks for Mobile Vision Applications. *ArXiv:1704.04861 [Cs]*.
<http://arxiv.org/abs/1704.04861>
- Lin, T.-Y., Maire, M., Belongie, S., Bourdev, L., Girshick, R., Hays, J., Perona, P., Ramanan, D., Zitnick, C. L., & Dollár, P. (2015). Microsoft COCO: Common Objects in Context. *ArXiv:1405.0312 [Cs]*. <http://arxiv.org/abs/1405.0312>
- Massa, F., & Girshick, R. (2018). *maskrcnn-benchmark: Fast, modular reference implementation of Instance Segmentation and Object Detection algorithms in PyTorch*. <https://github.com/facebookresearch/maskrcnn-benchmark/>
- MAY 6, J. S., & Read, 2020 6 Min. (2020, May 6). *What is Mean Average Precision (mAP) in Object Detection?* Roboflow Blog.
<https://blog.roboflow.com/mean-average-precision/>
- Merkel, D. (2014). Docker: Lightweight linux containers for consistent development and deployment. *Linux Journal*, 2014(239), 2.

- Neyshabur, B., Sedghi, H., & Zhang, C. (2021). What is being transferred in transfer learning? *ArXiv:2008.11687 [Cs, Stat]*.
<http://arxiv.org/abs/2008.11687>
- Neyshabur, B., Zhang, C., & Sedghi, H. (2020). *What is being transferred in transfer learning?*
- Nodjoumi, G. (2021, November 29). *DeepLandforms: First Release*. <https://doi.org/10.5281/zenodo.5734621>
- Paszke, A., Gross, S., Massa, F., Lerer, A., Bradbury, J., Chanan, G., Killeen, T., Lin, Z., Gimelshein, N., Antiga, L., Desmaison, A., Kopf, A., Yang, E., DeVito, Z., Raison, M., Tejani, A., Chilamkurthy, S., Steiner, B., Fang, L., ... Chintala, S. (2019). PyTorch: An Imperative Style, High-Performance Deep Learning Library. In H. Wallach, H. Larochelle, A. Beygelzimer, F. d'Alché-Buc, E. Fox, & R. Garnett (Eds.), *Advances in Neural Information Processing Systems 32* (pp. 8024–8035). Curran Associates, Inc. <http://papers.neurips.cc/paper/9015-pytorch-an-imperative-style-high-performance-deep-learning-library.pdf>
- PDS Geosciences Nodes. (2020). *PDS Geosciences Node Orbital Data Explorer (ODE)*. <https://ode.rsl.wustl.edu/>
- Pham, M.-T., Courtrai, L., Friguet, C., Lefèvre, S., & Baussard, A. (2020). YOLO-Fine: One-Stage Detector of Small Objects Under Various Backgrounds in Remote Sensing Images. *Remote Sensing*, 12(15), 2501. <https://doi.org/10.3390/rs12152501>
- Ren, S., He, K., Girshick, R., & Sun, J. (2016). Faster R-CNN: towards real-time object detection with region proposal networks. *IEEE Transactions on Pattern Analysis and Machine Intelligence*, 39(6), 1137–1149.
- Tan, C., Sun, F., Kong, T., Zhang, W., Yang, C., & Liu, C. (2018). A Survey on Deep Transfer Learning. *ArXiv:1808.01974 [Cs, Stat]*. <http://arxiv.org/abs/1808.01974>
- Targ, S., Almeida, D., & Lyman, K. (2016). Resnet in resnet: Generalizing residual architectures. *ArXiv Preprint ArXiv:1603.08029*.
- Tempfli, K., Huurneman, G. C., Bakker, W. H., Janssen, L. L. F., Feringa, W. F., Gieske, A. S. M., Grabmaier, K. A., Hecker, C. A., & Horn, J. A. van der. (2009). *Principles of remote sensing: An introductory textbook*. ITC.
- Weiss, K., Khoshgoftaar, T. M., & Wang, D. (2016). A survey of transfer learning. *Journal of Big Data*, 3(1), 9.
<https://doi.org/10.1186/s40537-016-0043-6>
- Wu, Y., Kirillov, A., Massa, F., Lo, W.-Y., & Girshick, R. (2019a). *Detectron2 is FAIR's next-generation platform for object detection, segmentation and other visual recognition tasks*. <https://github.com/facebookresearch/detectron2>
- Wu, Y., Kirillov, A., Massa, F., Lo, W.-Y., & Girshick, R. (2019b). *Detectron2/MODEL_ZOO.md at main · facebookresearch/detectron2*. https://github.com/facebookresearch/detectron2/blob/main/MODEL_ZOO.md
- Wu, Y., Kirillov, A., Massa, F., Lo, W.-Y., Girshick, R., & Facebook, Inc. (2020). *facebookresearch/detectron2: Detectron2 is FAIR's next-generation platform for object detection and segmentation*. <https://github.com/facebookresearch/detectron2>
- Zhang, A., Lipton, Z. C., Li, M., & Smola, A. J. (2021). 4.4.3 Underfitting or Overfitting? In *Dive into Deep Learning* (pp. 146–147). <http://arxiv.org/abs/2106.11342>